Wildfires front dynamics: 3D structures and intensity at small and large scales

Nicolas Frangieh, Gilbert Accary, Dominique Morvan, Sofiane Meradji, Oleg Bessonov

To cite this version:

Nicolas Frangieh, Gilbert Accary, Dominique Morvan, Sofiane Meradji, Oleg Bessonov. Wildfires front dynamics: 3D structures and intensity at small and large scales. Combustion and Flame, 2020, 211, pp.54-67. 10.1016/j.combustflame.2019.09.017 . hal-02892557

HAL Id: hal-02892557
https://hal.science/hal-02892557

Submitted on 21 Dec 2021

Wildfires Front Dynamics: 3D Structures and Intensity at Small and Large Scales

Nicolas Frangieh[1], Gilbert Accary[2], Dominique Morvan[1*], Sofiane Méradji[3], Oleg Bessonov[4]

[1] Aix-Marseille Université, CNRS, Centrale Marseille, M2P2, Marseille, France
[2] Scientific Research Center in Engineering, Lebanese University, Lebanon
[3] IMATH laboratory, EA 2134, Toulon University, France
[4] Ishlinsky Institute for Problems in Mechanics of the Russian Academy of Sciences, Russia

(*) Corresponding author (dominique.morvan@univ-amu.fr)

Abstract

The 3D structure of a fire front propagating through a homogeneous porous solid-fuel layer was studied numerically at laboratory and field scales. At laboratory scale, wind-tunnel fires propagating through laser-cut cardboard fuel were numerically reproduced, while at field scale, simulations of grassland fires with quasi-infinite fire front were carried out for different wind speeds. These simulations were performed using FIRESTAR3D, based on a multiphase formulation that includes the main physical phenomena governing fire behavior. An unsteady RANS approach and a Large Eddy Simulation (LES) approach were used to simulate the reactive turbulent flow, whereas turbulent combustion was modeled using Eddy Dissipation Concept (EDC). Unlike other 3D wildfire tools available in the community, such as FIRETEC and WFDS, the model is based on an implicit, low-Mach number resolution of the governing equations, and makes no empirical assumptions in the resolution of the radiative transfer equation. The comparison with the experimental data concerned mainly the Rate of Spread (ROS) of fire, the fireline intensity, the flame-zone depth, and the wavelength characterizing the crest-and-trough structure of the fire front along the transverse direction. Particular attention was drawn to the similitude in the fire front dynamics between small and large scales. In order to highlight the physical mechanisms responsible for this dynamics, a dimensional analysis was carried out by introducing Byram's convection number N_C based on the fireline intensity and Froude's numbers Fr based on the characteristic wavelength of the fire-front structure. The analysis shows that all the results (wind-tunnel fires and grassland fires, experimental and numerical) collapsed on a single scaling law in the form $Fr = N_C^{-2/3}$.

Keywords

Physics-based model, Fire spread, Front dynamics, Grassland fire, Wind-tunnel fire.

1. Introduction

For various reasons mainly related to climate changes and to the changes in the land use, such as the rural exodus and the extension of the wildland urban interface, wildfires has become an increasingly problematic natural risk, with each year a new collection of catastrophic events, one of the latest ones is the dramatic Camp Fire, in California in November 2018 [1]. A lot of experts agree about at least one point: even if the increase of firefighting means and the policy of fire exclusion in forest have contributed to reduce the number of fires, they have on the other hand contributed to the increase of the biomass and therefore of the intensity of wildfires. To summarize, during the last decades we have observed less fires but more intense fires. As recommended by many experts, a part of the solution to this problem, is certainly to do more in prevention policies and to engage the fire before it starts [2], as well as to develop programs of fuel load management as much as possible. In complement to these prevention actions, we must also do more research works in the understanding of the basic physical mechanisms governing the behavior of wildfires [3].

Even if it is well known that wind, fuel moisture content, and slope are certainly the main three factors affecting the behavior of wildfires, we also know that the level of correlation between these three factors and the parameters describing the fire dynamics, such as the rate of spread (ROS) and the fireline intensity, cannot be represented using a single relationship. This interdependency between the fire and the conditions of propagation is strongly affected by the regime of propagation, the forces acting on the trajectory of the flame, and the modes of heat transfer between the flame and the unburned fuel [4-7]. For surface fires, i.e. fires affected the understory vegetation (grasslands, shrublands), two regimes of propagation have been clearly identified, namely plume-dominated fires and wind-driven fires. The transition between these two regimes is piloted by the ratio between the two forces governing the trajectory of the flame: the buoyancy contributing to maintain the flame more or less vertical and the inertia due to the action of the wind pushing the flame horizontally towards the unburned vegetation. The ratio between the power of these two forces defines a dimensionless parameter, Byram's convective number [8], defined as follows:

$$N_C = \frac{2\,g\,I}{\rho_0\,C_{P0}\,T_0\,(U - ROS)^3} \tag{1}$$

where, ρ_0 and C_{P0} represent respectively the density and the specific heat of air in standard conditions at temperature T_0, g is the acceleration of gravity, I is the fireline intensity, and U and ROS are respectively the wind speed and the rate of spread of fire. The thresholds for the transition between the two regimes of propagation are: $N_C < 2$ (wind-driven fire, i.e. fire maintained near the ground and mainly piloted by the wind) and $N_C > 10$ (plume-dominated fire, i.e. fire developing a large plume and piloted by buoyancy effects) [7, 9]. By using the fire-line intensity (I in W/m), the Byram's convective number is a good indicator of the potential impact of a fire, evaluated locally at the fire front level, it is (from our point of view) a more pertinent parameter, compared to the flame height or flame length, used to evaluate Froude's number.

Many factors can contribute to the wind/fire interaction, such as the unsteady nature of the wind, the initial length of the ignition line, and the 3D structure of the fire front. Experimental fires performed in the field through a homogeneous fuel (grass) [10], confirmed by numerical simulations [11], have clearly highlighted that the rate of spread of the fire front does not have the same value for a point and a line ignition. For a line ignition, results showed that reaching a quasi-steady state value of the ROS required an ignition line length of at least 100 to 150 m long [10]. This phenomenon has been studied numerically, and the analysis of numerical results had shown that for a finite-length ignition line, the local flow at the vicinity of the two ends of the fire front affects negatively the flame length and, therefore, the heat transfer between the fire front and the solid fuel. This effect decelerates the propagation of the fire-front flanks in comparison to its center, resulting in a parabolic shape fire front [11, 12]. This phenomenon represents a real limitation for fire experiments on the field, because it means that it is necessary to perform quite large experiments with an ignition line more than 100-150 m long, in order to reach a quasi-equilibrium rate of spread. In addition, some numerical simulations have also shown that the ignition method could more or less contribute to increase this border effect [13]. To avoid this experimental artefact, numerical studies have been carried out using periodic boundary conditions along the two lateral sides [14]; this approach has the advantage to reproduce, at low cost, the 3D behavior of a quasi-infinite length fire-front. We know that fire front dynamics are strongly affected by 3D vertical structures, characterized transversely by a succession of crests and troughs. It has been shown experimentally, at small scale for fire spread through cardboard fuel-beds, that the characteristic wavelength of the fire-front structure scales directly with the flame height [15-17], and it was suggested that laboratory-scale fire spread processes should extend readily to full-scale field proportions, by proper scaling laws. On the other hand, both experimental observations and numerical simulations [18] have shown that horizontal structures are also present. Except under very rare conditions (homogeneous solid fuel, on a flat terrain, without wind), as already observed for a premixed flame [19] the fire front was never quite straight; instead, the fire front was structured horizontally by more or less pronounced wrinkles. This comparison between premixed gaseous flame and wildfires is not really surprising considering that, at large scale, the behavior of a fire front has many similarities with the propagation of a premixed gaseous flame, with the vegetation playing the role of the gaseous fuel. . Sayed differently, in a wildfire the fuel (the vegetation) and the oxygen (the ambient atmosphere) are naturally mixed, similarly as for a premixed flame. A consequence of that is, as for a premixed flame we can observe a propagation of a flame front through the vegetation layer with a structuration of the front (wrinkles) resulting from the interaction between the flame and the atmospheric flow. Of course other aspects of the physics are different, but there exists some similitude between premixed flame and wildfire front. Even if 2D numerical simulations have highlighted the general trends concerning the effects of the wind speed, of the fuel moisture content, and of the slope, on the behavior of wildfires [4, 5, 20], their main flaw seems to be the overestimation of the wind effect on the flame and plume trajectory. In 2D, the fire front acts as a uniform thermal barrier, and the incoming wind flow has no other choice than to push the flame downstream (toward the unburned vegetation) whereas in 3D, the trough between two fire-front crests allows the wind flow to cross the fire front, contributing to rectify the flame and the plume trajectory [18].

In order to study 3D effects in wildfires behavior and to check the validity of the scaling laws between the fire-front properties, we propose in this paper to simulate numerically, using a multiphase fully-physical fire model (FIRESTAR3D) [13, 21], the propagation of a fire front at a small scale and at a large scale. At a small scale, duly chosen experiments of fire spread through cardboard fuel-beds, carried out in wind tunnel at Missoula Fire Sciences Laboratory [16, 17], are modeled and reproduced numerically. In addition to the ROS, these studies report the observed characteristic wavelengths of the fire-front, the horizontal flame-zone depth, and the characteristic frequencies of the flame fluctuations recorded by thermocouples. Thus, reproducing these experiments comes also in the framework of FIRESTAR3D validation. At a large scale, simulations of grassland fires with a quasi-infinite fire front are carried out using periodic conditions on the lateral vertical boundaries of the computational domain.

2. Modeling and Numerical model

The mathematical model used in FIRESTAR3D is based on a multiphase formulation [22], it consists in a first step in space-averaging the conservation equations (mass, momentum, energy …) governing the behavior of the coupled system formed by the vegetation and the surrounding atmosphere. This averaging is performed on elementary control volumes including both the solid phase (the vegetation) and the gaseous phase. This first operation, similar to a homogenization step, results in the introduction of source/sink terms on the right hand side of the equations, representing the contributions of the interaction terms (exchanges of mass, drag, heat flux …) between the gaseous phase and the vegetation. The details of the model have been widely presented in previous publications [21, 23–26], we invite the reader to consult reference [21] for more information about the 3D model and for a comparison with other 3D wildfire tools available in the community such as FIRETEC [14] and WFDS [11].

The model consists of two parts that are solved on two distinct grids. The first part consists of the equations of a reacting turbulent flow in the gaseous phase composed as a mixture of fresh air with the gaseous products resulting from the degradation of the solid phase (by drying, pyrolysis, and heterogeneous combustion) and the homogeneous combustion in the flaming zone. The second part consists of the equations governing the state and the composition of the solid phase subjected to an intense heat flux coming from the flaming zone.

In all simulations, we have considered that the state of the solid-fuel particles can be represented by a single temperature and that the possible small gradient of temperature within the particle does not play a significant role in the fire dynamics at these scales (thermally thin assumption). Indeed, the results showed that the average Biot number during the pyrolysis phase of the solid-fuel degradation (for a temperature range between 400 and 500 K) was about 0.07 in the case of cardboard fires and 0.6 in the case of grassland fires. Even though the thermally thin hypothesis (Biot < 0.1) was not fully verified in the case of grassland fires, we consider that the degree of complexity in our model was sufficient without accounting for a gradient of temperature within the solid-fuel particles. On the other hand, we believe that the size of fuel particles (thickness < 1 mm) does not justify the additional effort required to account for an inner temperature gradient in order to improve significantly the quality of our simulations. Finally, assuming a homogeneous temperature within the solid-fuel particles may be assimilated to an averaging process.

Solving the gaseous phase model consists in the resolution of conservation equations of mass, momentum, energy (in enthalpy formulation), and chemical species (O_2, N_2, CO, CO_2, and H_2O) filtered either in time using an unsteady RANS approach (URANS), either in space using a Large Eddy Simulation approach (LES), with Favre average formulation [27]. The closure of the averaged conservation equations is based on the eddy viscosity concept [28] obtained from an evaluation of the turbulent kinetic energy k and its dissipation rate ε. In the case of the URANS approach, a high Reynolds number version of a two-equation statistical turbulence model (k-ε) used with the RNG formalism [29, 30], while a high-order sub-grid scale stresses model [31] is used in the case of the LES approach. The temperature dependence of the gas-mixture enthalpy is based on CHEMKIN thermodynamic tables [32]. A combustion model based on Eddy Dissipation Concept (EDC) [28, 33] is used to evaluate the combustion rate occurring in the gaseous phase. Finally, because radiation heat transfer (mainly due to the presence of soot particles in the flame) plays an important role for the propagation of the fire front, the field of soot volume-fraction in the gas mixture is calculated by solving a transport equation [34, 35] including a thermophoretic contribution in the convective term and taking into consideration soot oxidation [36].

Concerning the solid phase model, during the thermal degradation, the composition of the solid fuel particles representing the vegetation is represented as a mixture of dry material (generic term for a mixing of cellulose, hemicellulose, and lignin), charcoal, moisture, and residual ashes. For each solid particle, the model consists in solving the equations governing the time evolutions of the mass fractions of water, of dry material, of charcoal, as well as of the total mass of the solid particle, its volume fraction and its temperature (the model does not assume a thermodynamics equilibrium between the gas mixture and solid fuel particles). The degradation of the vegetation is governed by three temperature-dependent mechanisms: drying, pyrolysis, and charcoal combustion. The pyrolysis process starts once the drying process is completed and charcoal combustion starts once the pyrolysis process is achieved. The constants of the model associated with the charcoal combustion (activation energy and pre-exponential factor) are evaluated empirically from a thermal analysis conducted on various solid fuels samples [22, 37].

The interaction between the gaseous phase and the solid one is taken into account through coupling terms that appear in both parts of the model. These terms are linearly interpolated between the fluid-phase and solid-phase grids. The coupling in the momentum and turbulence equations is obtained by adding aerodynamic drag terms. These terms (both source and sink) are proportional to V (for turbulence destruction), to V^2 (for the momentum equation), and to V^3 (for turbulence production), where V is the local average of the velocity magnitude [25], and include a drag coefficient (evaluated empirically) multiplied by a reference surface, defined here as the Leaf Area Density (LAD). Heat transfer between the gas mixture and the solid fuel is based on empirical correlations for convective transfer coefficient [37], and on the resolution of the radiative transfer equation [38] that accounts for the presence of soot in the flaming zone and for the presence of hot particles in the vegetation layer (embers) [22]. Finally, mass transfer from the solid phase to the gaseous phase is represented by adding source/sink terms in the mass conservation equations of both phases.

The balance equations in the gaseous phase are solved numerically using a fully implicit finite volume method in a segregated formulation [39, 40]. FIRESTAR3D model predicts turbulent reacting flows in rectangular domains using a structured but non-uniform staggered mesh. Time discretization relies on a third order Euler scheme with variable time stepping strategy. To ensure numerical stability, space discretization is based on second order schemes with flux limiters (QUICK scheme [40, 41]) for convective terms while diffusion terms are approached by central difference approximation with deferred corrections [42] to maintain the second order accuracy in space. The Radiative Transport Equation (RTE) is solved using a Discrete Ordinate Method (DOM), consisting in solving the radiation-intensity equation in a finite number of directions [43]. The radiative transfer equation accounts for gas-soot mixture absorption of radiative intensity depending on the amounts of combustion products (CO_2 and H_2O), on the gas mixture temperature, and of the soot volume fraction [44]. This set of discrete contributions is then integrated using a numerical Gaussian quadrature rule (a S_8 method is used) for the calculation of the total irradiance. The set of ordinary differential equations describing the time evolution of solid-fuel state (mass, temperature, and composition) are solved separately using a fourth order Runge-Kutta method. From implementation point of view, the computation code is parallelized [45] and optimized [46] using OpenMP directives (operational on shared memory high-performance computing platforms and on Intel Xeon Phi coprocessors). Finally, the hydrodynamic module of the code has been extensively validated on several benchmarks of laminar and turbulent natural convection, forced convection, and neutrally stratified flow within and above a sparse forest canopy [47–50]. The predictive potential of Firestar3D model has also been estimated at small scale in the case of litter fires in well-controlled experimental conditions (fire propagation through a homogeneous fuel-bed in a wind tunnel) [21] and at a larger scale for grassland fires (experimental campaign carried out in Australia) [13].

3. Fire spread in engineered cardboard fuel-beds

3.1. Experimental fires results

Fires spreading through uniform cardboard fuel-beds were conducted and analyzed at Missoula Fire Sciences Laboratory in a 3 m × 3 m cross-section wind tunnel [16, 17]. Using 1.397 mm-thick cardboard, laser-cut fuel-particles were created at different lengths and widths and arranged at different row spacing (as shown in Fig. 1) to achieve specific fuel-bed properties: fuel-bed height δ (2.5 to 35.6 cm), fuel volume fraction α_S (0.00267 to 0.0116), surface-to-volume ratio σ_S (2297 to 3818 m^{-1}). Such fuel-bed properties cannot be easily reproduced with other solid fuels usually used in laboratory, such as pine needles and excelsior [51]. Indeed, by producing sparse solid-fuel layer, the use of laser-cut cardboard seems to be the easiest way to obtain conditions quite similar to those encountered in wildfires. In all, 28 experiments were conducted for different wind speeds U (between 0.22 and 1.5 $m.s^{-1}$) and different fuel-bed width Y (between 0.914 and 2.438 m). Fire characteristics were analyzed using 64 thermocouples arranged in a single line in the direction of fire spread. These thermocouples were used to evaluate the ROS as well as the frequency of the observed flame fluctuations. In addition, the study reported a rough estimation of the fire-front height, the horizontal flame-zone depth, and the characteristic wavelength of the fire-front in crests and troughs (as shown in Fig. 2). Note that figures 1 and 2 actually represent the experimental setup for a fire table (used to study the slope effect), they are however fully representative of the fuel structure (Fig.1) and of the shape of the flame front (Fig. 2) observed in the wind-tunnel experiments. In some manner, this experimental configuration [16, 17] has allowed to explore at laboratory scale some features concerning fire dynamics that were only observed on the field, with the main advantage to do that with fully controlled conditions. The study [17] showed that the characteristic wavelength of the fire-front structure scaled directly with its height. It revealed particularly a direct relationship between Strouhal's and Froude's numbers based on the flame fluctuations characteristic-frequency, the wind speed, and the flame height. It also showed that the downstream extent of these fluctuations scaled with Froude's number and the horizontal flame-zone depth. These behaviors are remarkably similar to those observed in buoyancy-dominated wildland fire spread, suggesting that laboratory-scale fire spread could extend readily to full-scale field proportions, by proper scaling laws. Unfortunately, an error analysis was not possible because it was not reported in the experimental study [16, 17].

Fig. 1. Picture of the laser-cut cardboard laboratory fuel-bed used in [16, 17] (Photo by D. Morvan at the Missoula Fire Sciences Laboratory), with a line of alcohol-imbibed excelsior (in the foreground) added for the ignition of the cardboard bed.

Fig. 2. Typical crest-and-trough structure of 2-m high flame observed in [16, 17] (Photo by D. Morvan at the Missoula Fire Sciences Laboratory).

3.2. Numerical modeling

The computation domain corresponding to the experiments of fire spread in cardboard fuel-beds is shown in Fig. 3. The fuel-bed was divided into two zones having the same physical characteristics; however, only zone (2) was thermally degradable. Zone (1) (2 m long) was added to account for the presence of a wire mesh spoiler used in the experiment, arranged in Z-folds, and placed on the floor of the wind tunnel transversely from wall to wall, to initiate more rapidly the turbulent boundary layer flow. Also, in the experiments, the sides of the fuel-beds were lined with paper (matching the fuel-bed height) that was treated with flame retardant to mimic a wider fire front by preventing in-drafts into the combustion zone. These paper sheets were accounted for numerically by placing vertical baffles along each side of the fuel-bed (see Fig. 3); the velocity component normal to the baffles (y component) was set to zero, while a friction coefficient $C_f = 0.01$ was introduced in the momentum equations of the velocity components tangential to the baffles (x and z components). This friction coefficient is twice that of a turbulent flow over a smooth flat plate (to account for both sides of the baffles) at a Reynolds number of about 5×10^5. Nevertheless, doubling the value of C_f or dividing it by 2 had no noticeable effect on the fire dynamics.

Before ignition, simulations were run long enough using Neumann conditions at the open boundaries while imposing a negative artificial pressure gradient in the x-momentum equation. This artificial pressure gradient was adjusted automatically by the solver in order to reach at each time step the desired wind speed at the center of the wind tunnel entrance that was imposed in the experiment. This phase was maintained for 5 seconds, which was the time required for reaching a quasi-steady turbulent flow. Then, the turbulent velocity profile, obtained at the wind tunnel entrance, was applied at the inlet of the domain during the remaining time of simulation. At t = 5 s, fire was set at the entrance of zone (2) by injecting carbon monoxide at 1600 K from the bottom of the computation domain for another 5 seconds. This CO jet reacts with O_2 in the ambient air producing CO_2 and the required heat to start solid-fuel combustion, hence reproducing a porous gas burner. The injection surface lies between x = 2 m and x = 2.16 m, and along the entire width of zone (2). According to Eq. (2), at t = 5 s the average injection speed is maximum (V_j = 10 cm.s^{-1}), then it decreases linearly with the burned mass of dry material (m_b) in order to avoid destabilizing the fire-front by suddenly ceasing the injection.

$$V_j(cm.s^{-1}) = 10 \times \left(1 - \frac{m_b}{m_{b0}}\right) \tag{2}$$

where m_{b0} is the initial mass of dry material located above the burner (i.e. the mass of dry material inside the volume $V_{b0} = 0.16\times1\times\delta$ m^3). Equation (2) was used between t = 5 s and t = 10 s as long as V_j had remained positive, but the injection of carbon monoxide was stopped once V_j had reached zero during this time interval.

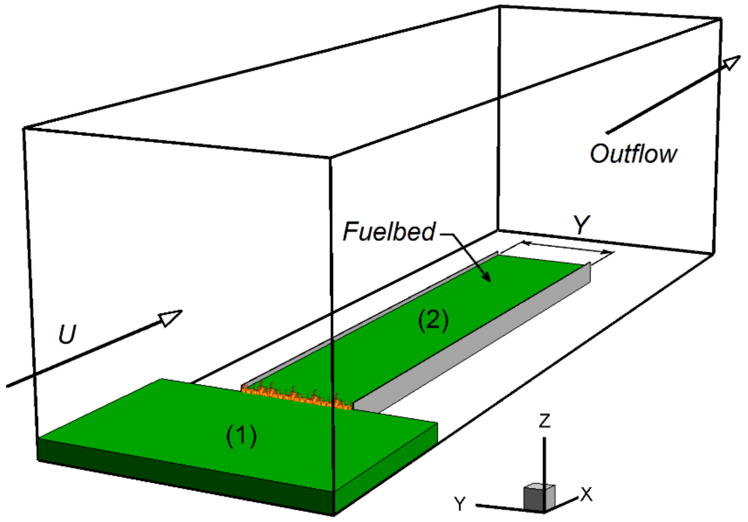

Fig. 3. Perspective view of the computation domain corresponding to the experiments of fire spread in engineered cardboard fuel-beds. The flow domain dimensions are 10×3×3 m^3 and those of the fuel-bed are $8 \times Y \times \delta$ m^3 (the fuel-bed thickness $\delta = 20.3$ cm). The fuel-bed is divided into two zones, only zone (2) (2m < x < 8m) is thermally degradable, vertical baffles (0.203 m high) are placed along both sides of zone (2) and fire is set at its entrance.

Among the 28 reported experiments [16, 17], six experiments were duly chosen for numerical simulation to include three effects: the wind velocity U, the transverse width of fuel-bed Y, and the volume fraction of the solid phase α_S. These six experiments (10, 18, 19, 24, 25, and 26), whose physical properties are shown in Tab. 1, were chosen because their fuel-bed height (δ= 20.3 cm) was large enough to contain several grid points, thus allowing a good description of the flow within the fuel-bed. For these experiments the fuel-particles widths (normal to wind direction) w = 2.3114 mm [52], which results for rectangular cross-sectional particles in a surface-to-volume ratio $\sigma_S = 2297$ m^{-1}, according to Eq. (3) with an aspect ratio (length-to-width) $AR = 1.397/2.3114 = 0.6044$. The simulations were conducted using the following air condition at the wind tunnel entrance: dry-bulb air temperature of 15°C, relative humidity of 25%, and intensity of turbulence of 10%. In addition, the fuel-particles material is characterized by a dry cardboard density $\rho_S = 600$ kg.m^{-3}, a moisture content of 8%, and a pyrolysis heat $\Delta H_{pyr} = 570$ kJ.kg^{-1} [52].

$$\sigma_S = \frac{1 + AR}{AR} \times \frac{2}{w} \tag{3}$$

Exp. No. as in [17]	U (m.s^{-1})	α_S	Y(m)
10	0.22	0.00535	1.219
18	0.44	0.00897	1.829
19	0.67	0.00897	1.829
24	0.89	0.00897	2.438
25	0.44	0.00535	2.438
26	0.44	0.00385	2.438

Tab. 1. Physical input data of the considered experiments of fire spread in cardboard fuel-beds: U (wind speed), α_S (solid-fuel volume fraction), Y (transverse width of fuel-bed).

The laws of friction and heat transfer for a flow across rectangular cylinder are not available in the literature for any aspect ratio. Therefore, correlations for the drag coefficient C_D and the forced-convection Nusselt number Nu_{FC} based on the particle width w were established, using data available for $AR = 0.5$, 1, and 1.5, and for a Reynolds number Re varying from 25 to 10^4 [52–54]. These correlations, given by Eqs. (4) and (5), depend on the Reynolds number based on the particle width w and gas-mixture Prandtl number Pr, where coefficients $A = 8.970$, $B = 2.437$, and $C = 0.3515$ for $AR = 0.6044$. Note that these correlations were derived using steady-flow data and do not account for rapidly changing flow conditions (Reynolds number and flow direction) across the cardboard-fuel particles. Note also that these correlations do not account for particle-particle interaction, this effect is assumed to be marginal given the sparse nature of the cardboard fuel-bed. It should be also noted that Eq. (5) does not account for natural convection around the fuel particles, which is approximated in the case of vertical rectangular cylinders by natural convection along a vertical plate of length δ. Natural-convection Nusselt number Nu_{NC} is hence determined in terms of Rayleigh number [37]. Finally, the average Nusselt number used to determine the heat transfer coefficient is obtained from $Nu = \sqrt{Nu_{FC}^2 + Nu_{NC}^2}$ [21].

$$C_D = \frac{A}{Re^{0.407}} + B \times (1 - e^{-0.0016Re}) \tag{4}$$

$$Nu_{FC} = \mathrm{C}\, Re^{0.5636}\, Pr^{1/3} \tag{5}$$

At the end of the solid-fuel decomposition, when ash state has been reached, we have assumed that the drag force and the rate of heat transfer were both reduced to zero.

The unsteady RANS approach (URANS) with the RNG k-ε turbulence model was used in the resolution of conservation equations of mass, momentum, energy, and chemical species. A uniform mesh was used for the solid domain with a grid size (Δx, Δy, Δz) = (2 cm, 1.25 cm, 1.69 cm), while a wall-refined mesh of 250×96×62 grid points was used for the fluid domain, where the distribution of the 96 grid points in the transverse y direction depended on the fuel-bed width Y. Within the vegetation zone, the fluid-domain mesh was uniform and twice as coarse as the solid-domain mesh, whereas it was gradually refined toward the rigid walls. The fluid-domain grid size varied between 2.5 cm and 8.7 cm and respected the constraint $11.5 < y^+ < 500$ during the entire simulations time. In addition, the constraint given by $\Delta x < 4/\alpha_S\sigma_S$ [6] (grid size smaller than the extinction length scale) was respected in all directions for all simulations in order to avoid fire extinction within the fuel-bed for radiation-dominated fire propagation. For the adaptive time-stepping strategy, the minimum and maximum time-step values were set to 0.001s and 0.01s respectively, and the desired level of time discretization truncation error was set to 10^{-4}. Finally, at each time step, the global convergence was assumed to be reached when the L_2-norms of all transport equations residuals had reached 10^{-5} in normalized form. Typically, 30 seconds of simulation time required in average 75 hours of CPU time on a 24-processor shared-memory workstation.

As mentioned in the introduction, the comparison between the numerical simulations and the experiments was based on the ROS, the characteristic frequency f of the flame fluctuations, the flame-zone depth D, and the wave number $n_w = Y/\lambda$ corresponding to the wavelength λ characterizing the fire-front structure. The mesh effect was checked in the case of Exp. 24 (highest wind speed) by refining and coarsening the considered mesh by 25%. While the coarser mesh resulted in appreciable difference in the ROS and the frequency f reaching 11% and 12% respectively, the relative difference in the case of the finer mesh did not exceed 2% for both quantities. A wave number $n_w = 2$ was obtained for the three considered meshes.

3.3. Results and discussion

Figure 4 shows the flame patterns obtained numerically in the case of Exp. 24 ($U = 0.89$ m.s^{-1}) at 5 s time interval. We notice the crest-and-trough structure of the fire front, with a wave number $n_w = 2$, and the clear tilt of the flame in the wind direction. The flame structure and the flow field in the case of Exp. 24 ($U = 0.89$ m.s^{-1}) are further clarified by Figs. 5, 6, and 7. We notice in Fig. 5(a) that the fire front in the vertical median plane creates a barrier preventing the flow of the gas mixture, we notice also the existence of a reverse flow drawing in fresh air from the wind-tunnel exit into the flaming zone. This shows the potential of FIRESTAR3D in handling backflow situation (i.e. the model allows for a backflow to occur at the exit of the wind-tunnel as a result of the mass balance). The flow of the gas mixture between the fire-front crests is very clear in Figs. 5(b) and 5(c).

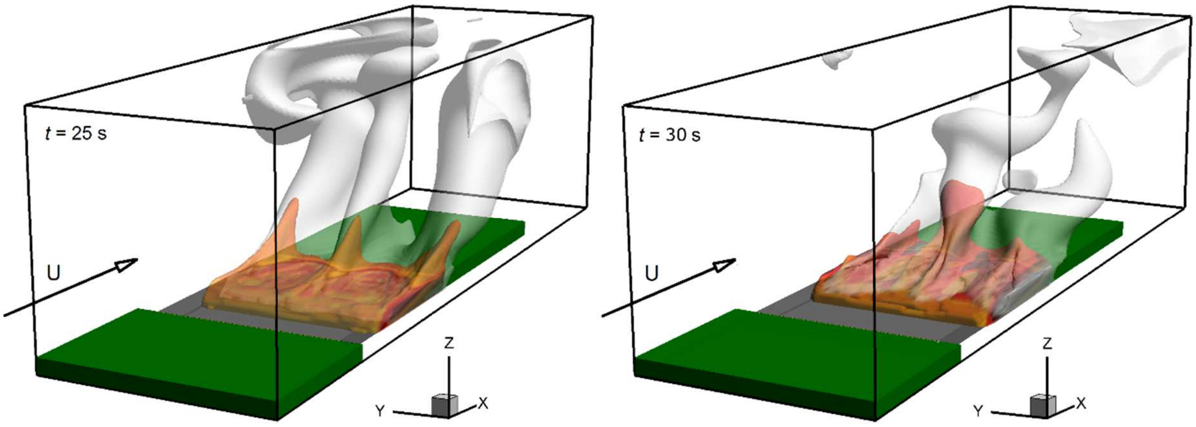

Fig. 4. 3D view of an isovalue surface of the soot volume fraction (10^{-7}) colored by the gas temperature (in yellow) and an isovalue surface of the water mass fraction (0.0075) (in grey with 50% of transparency) obtained in the case of Exp. 24 at *t* = 25 s and *t* = 30 s.

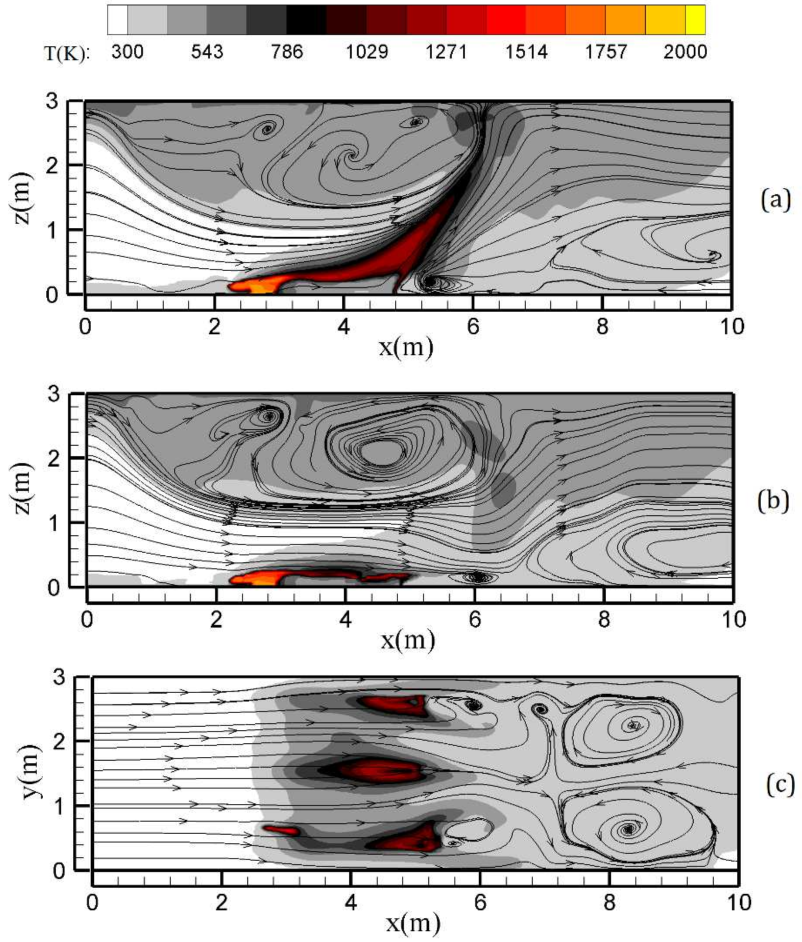

Fig. 5. Temperature fields and streamlines obtained numerically at *t* = 25 s in the case of Exp. 24 (see Tab. 1 for more details). (a) solution in the vertical median plane (*y* = 1.5 m), (b) solution in the vertical median plane (y = 2 m), (c) solution in the horizontal plane at $z = 2\delta$.

Figure 6 particularly highlights the acceleration of the gas mixture between the flame with a velocity reaching 3 m.s^{-1} for a wind speed of 0.89 m.s^{-1} at the wind tunnel inlet. By comparing the flow structure between Fig.5(a) and Fig.5(b), we can notice that the great heterogeneity of the fire front, characterized by a succession of crests and troughs, allowed for the incoming air flow to cross the fire front (see also Fig.5(c)), this feature illustrates again the interest of performing 3D simulations. Figure 7 particularly highlights the existence of a pair of longitudinal roller vortices through the fire front (similar to Görtler vortices observed for a boundary layer flow on a curved surface) that contribute significantly to the fire behavior and spread by creating downwash and upwash zones where the vortex pair converge, as explained and highlighted experimentally in [16, 17].

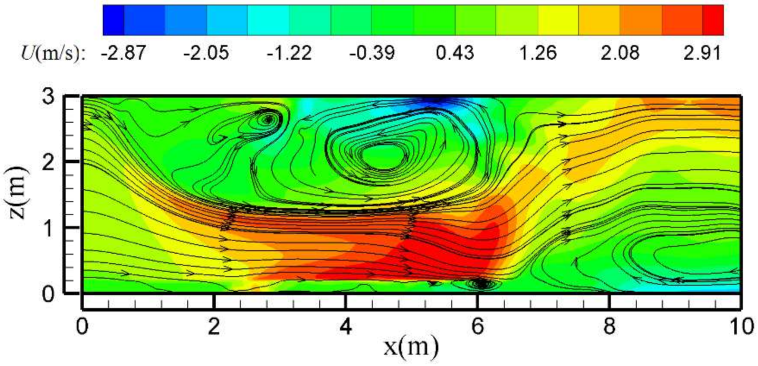

Fig. 6. Velocity component in the *x*-direction and streamlines obtained numerically at $t = 25$ s in the vertical median plane ($y = 1.5$ m) in the case of Exp. 24, for a wind speed of $U = 0.89$ m.s^{-1}.

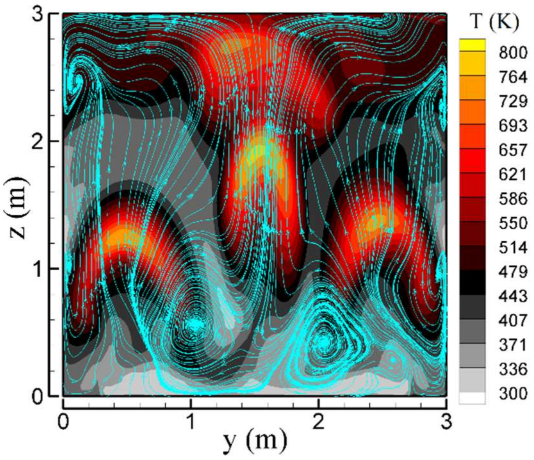

Fig. 7. Temperature field and streamlines in the vertical plane at $x = 6$ m, obtained at $t = 25$ s in the case of Exp. 24 (see Tab. 1 for details).

As shown by Fig. 8, the pyrolysis front obtained in the case of Exp. 24 is shaped by the fire-front structure and the associated flow field. The hot gases passing between the fire front, as a pair of roller vortices, initiate the combustion of the solid fuel. We notice the remote dehydration process due to radiation ahead of the fire front, and we notice also that the pyrolysis process takes place within the upper layer of the fuel-bed first, before affecting the entire solid-fuel layer. A similar behavior was highlighted in [16], where the tops of cardboard tines ignited first. Finally, figure 8 shows that the charcoal area spreads over 2 m at the fuel-bed surface, while it has a much smaller extent within the fuel-bed.

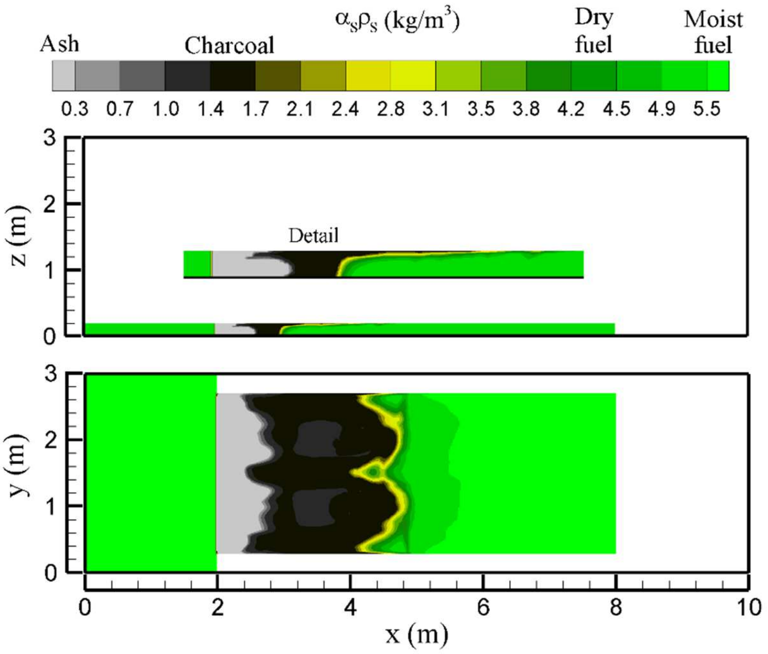

Fig. 8. Distributions of the fuel-bed density ($\alpha_S\rho_S$) at the surface of the fuel-bed (z = 0.203 m) and in the vertical median plan (y = 1.5 m), obtained at t = 25 s, corresponding to Exp. 24 (see Tab. 1 for details).

To understand the effect of the wind speed on the flame structure, figure 9 shows the flame patterns obtained numerically in the case of Exp. 10 (U = 0.22 m.s^{-1}). Compared to Fig. 4 (Exp. 24 with U = 0.89 m.s^{-1}), the flame is vertical in the case of Exp. 10, and due to the smaller width of the fuel-bed, the fire front is not showing a noticeable structure (n_w = 1) as in Exp. 24 (see Tab.2).

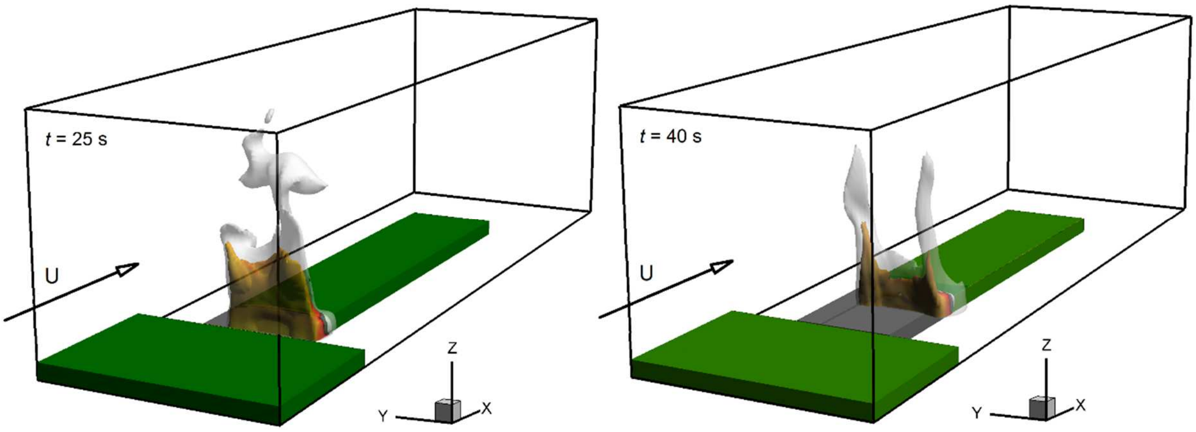

Fig. 9. 3D view of an isovalue surface of the soot volume fraction (10^{-7}) colored by the gas temperature (in yellow) and an isovalue surface of the water mass fraction (0.0075) (in grey with 50% of transparency) obtained in the case of Exp. 10 at t = 25 s and t = 40 s.

The flame structure and the flow field in the case of Exp. 10 (U = 0.22 m.s^{-1}) are further clarified by Fig. 10. A vertical fire front slightly tilted backward is observed in the vertical median plane (y = 1.5 m), and we notice the existence of an important reverse flow, drawing in fresh air from the wind-tunnel exit into the flaming zone. This behavior is not so surprising, in no wind or weak wind conditions. Furthermore, for a relatively-high rate of spread (resulting from quite low levels of fuel moisture-content) the propagation of the fire front also contributes to the deviation of the plume in the opposite direction fire propagation. This vertical fire front constitutes a barrier that deviates vertically the incoming air that flows along the top wall of the wind tunnel at high speed reaching about 4 m/s in the case of Fig. 10(a).

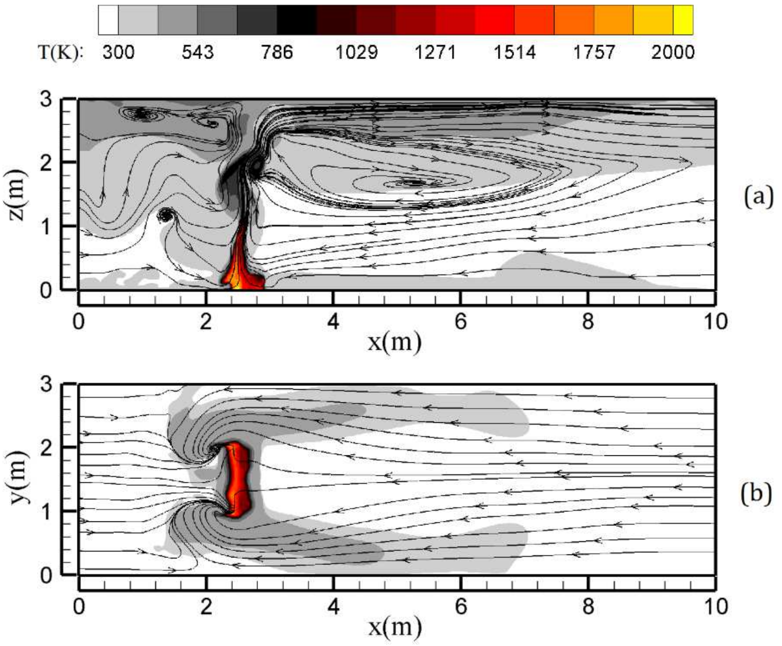

Fig. 10. Temperature fields and streamlines obtained numerically at $t = 25$ s in the case of Exp. 10 (see Tab. 1 for more details). (a) Numerical solution in the vertical median plane ($y = 1.5$ m), (b) solution in the horizontal plane at $z = 2\delta$.

To better understand the heat balance at the fuel particles, figures 11 and 12 show the time evolution of thermal properties at location ($x = 4$ m, $y = 1.5$ m, $z = \delta$), i.e. at the fuel-bed surface and 2 m from the ignition line. On the time evolution of the fuel-particle temperature (Fig. 11), we notice the water-evaporation plateau at 373 K, followed by the pyrolysis phase between 400 K and 500 K according to the model [21], then char combustion raising the particle temperature for a fraction of second up to 2500 K (the adiabatic flame temperature of CO combustion). On the time evolution of the gas-mixture temperature, we clearly notice the heating fluctuations ahead of the fire front (between 10 and 25 s) observed experimentally (recorded by thermocouples signals at many locations), resulting from a secondary hydrodynamic instability of the roller vortices, as pointed out in [16, 17]. As shown by Fig. 12, ahead of the fire front (for $t < 25$ s), the fuel particles are heated up by convection and radiation equally (the heat fluxes absorbed by convection and radiation are comparable). The particles also lose heat by convection and radiation equally during the first seconds of combustion (between 25 and 30 s). However, during the few seconds of extreme temperature, combustion energy absorbed by the fuel particle is mainly evacuated by radiation. More details about the thermal equilibrium of the fuel particles can be found in [21].

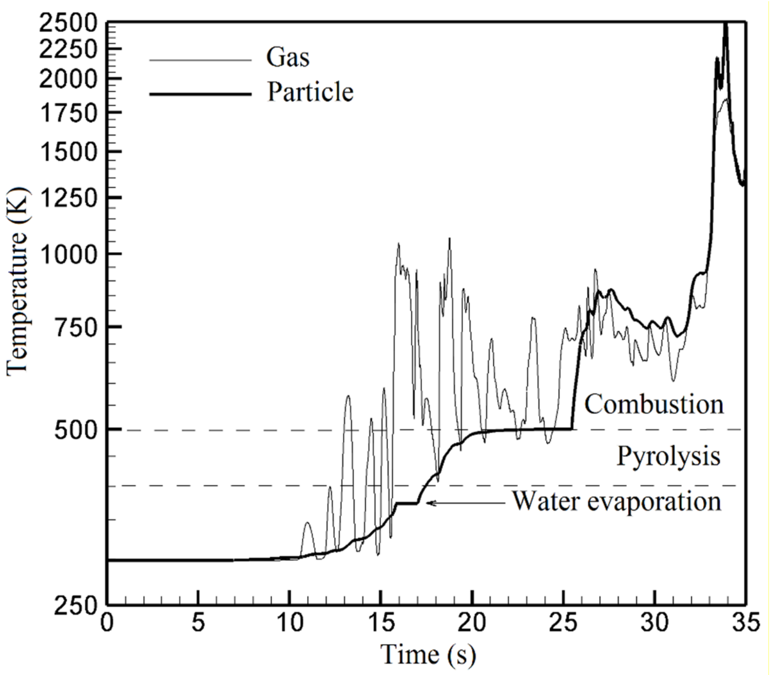

Fig. 11. Time-evolution of the fuel particle and the gas-mixture temperature at location ($x = 4$ m, $y = 1.5$ m, $z = \delta$), obtained numerically in the case of Exp. 24.

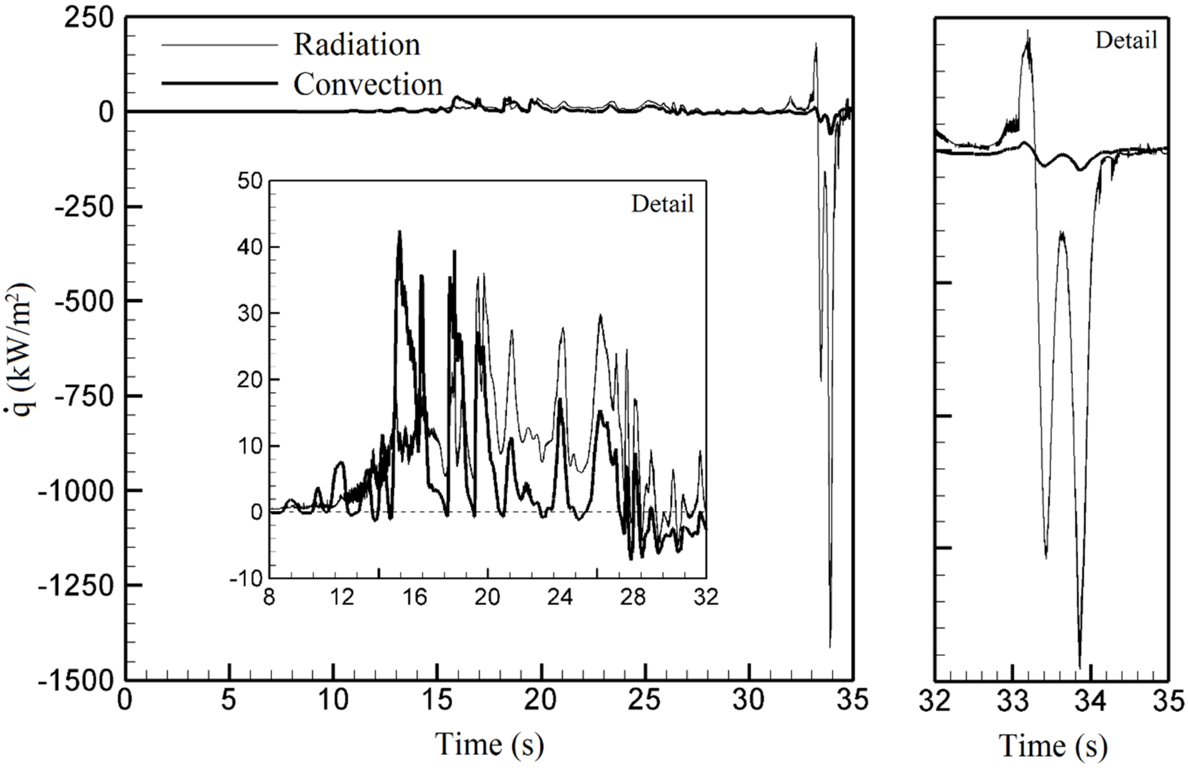

Fig. 12. Time-evolution of the convection and radiation heat fluxes absorbed by the fuel particle at location ($x = 4$ m, $y = 1.5$ m, $z = \delta$), obtained numerically in the case of Exp. 24. Negative values correspond to heat loss form the fuel particle.

The ROS may be evaluated at the centerline of the fuel-bed surface by measuring the required time for the pyrolysis front to move from a position to another along line ($y = 1.5$ m, $z = \delta$), as in the experiments [16, 17]. However, a simpler and more accurate method for estimating the

ROS consists in finding at each time step of simulation the average position of the pyrolysis front at the fuel-bed surface. The ROS was then obtained from Fig. 13, by evaluating the slope of the curve once fire propagation had become steady, and reported in Tab. 2 for all considered cases. We notice that FIRESTAR3D predicts the correct order of magnitude of the ROS (except for Exp.10 – lowest wind speed) and the correct dependence on the wind speed. Indeed, cases 18, 19, and 24 share the same fuel-bed volume fraction $\alpha_S = 0.00897$ (see Tab. 1), but have different wind speeds (0.44, 0.67, and 0.89 $m.s^{-1}$ respectively); we notice that the ROS estimated by simulation increases with the wind speed. A possible reason for the overestimation the ROS observed at low wind speeds is the overestimation of the radiative heat transfer from the walls of the wind tunnel that are assumed to behave as insulated black surfaces (no heat loss by radiation), which is surely not the case in these experiments; in addition, one of the vertical walls contains a very large window to allow fire visualization.

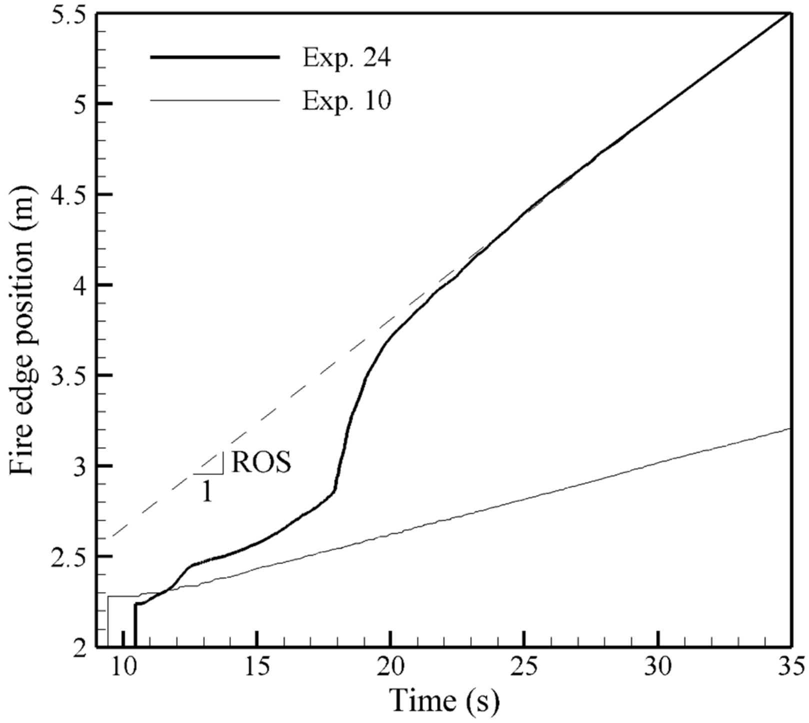

Fig. 13. Time-evolution of the average fire edge position at the fuel-bed surface in the case of Exp. 10 and Exp. 24 (see Tab. 1 for details). The ROS is the slope of the curve at steady fire propagation.

Fire intensity was estimated from the heat release rate (HRR) given by Eq. (6) where ω_{vap}, ω_{pyr}, ω_{char}, ω_{CO} and ω_{soot} are respectively the total mass rates of water evaporation, pyrolysis, char combustion, combustion of CO in the gas mixture, and soot combustion, and ΔH_{vap}, ΔH_{pyr}, ΔH_{char}, ΔH_{CO} and ΔH_{soot} are the corresponding specific heats.

$$HRR = -\omega_{vap}\,\Delta H_{vap} - \omega_{pyr}\,\Delta H_{pyr} + \omega_{char}\,\Delta H_{char} + \omega_{CO}\,\Delta H_{CO} + \omega_{soot}\,\Delta H_{soot} \qquad (6)$$

Note that ΔH_{char} is not constant, it depends on the proportion of CO to CO_2 produced during charcoal combustion [21], it varies between 9 $MJ.kg^{-1}$ (for an incomplete combustion) and 30 MJ/kg (for a complete combustion). As shown in Fig. 14, the HRR reaches a quasi-constant average value at steady state fire propagation and shows clear fluctuations. These fluctuations of the overall rate of heat released by the flame in the entire domain naturally correlate to the average of the temperature fluctuations recorded by thermocouples at different locations in the experiment and reproduced numerically in Fig. 11. The dominant frequency f of these fluctuations was determined by Fourier transform of the heat release rate signal (shown in Fig. 14) and is compared in Tab. 2 to the frequency of flame fluctuations observed experimentally. For all the considered cases and all the analyzed variables (rate of spread, frequency, fire front depth), we globally notice a good agreement between experimental data and numerical values. The fireline intensity (investigated in section 5) is obtained from $I = HRR_{ss}/Y$, where HRR_{ss} is the average value of the heat release rate obtained at steady state.

Tab. 2 compares also the wave numbers (time-averaged values), characterizing the crest-and-trough structure of the fire front, observed numerically and experimentally, where a good agreement is globally obtained for this fire property also.

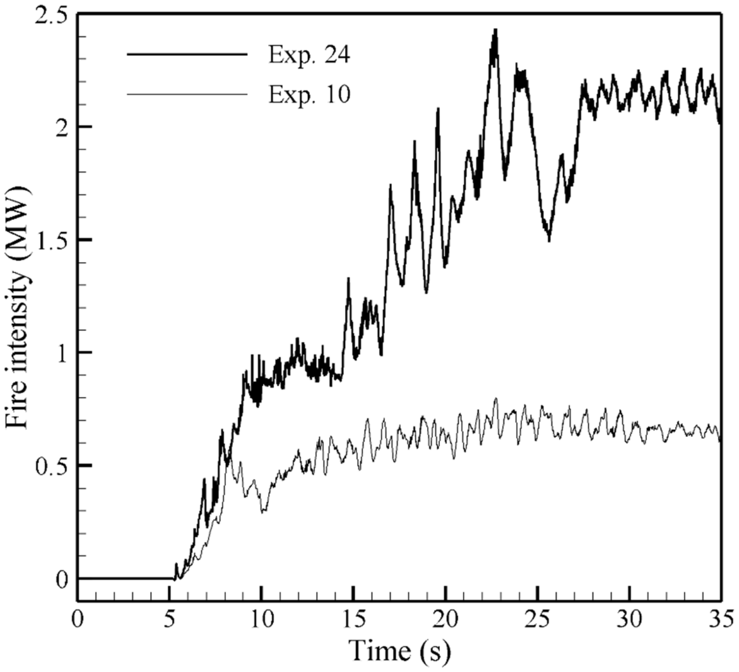

Fig. 14. Time-evolution of the heat release rate in the case of Exp. 10 and Exp. 24 (see Tab. 1 for details).

Finally, the values of the horizontal flame-zone depth D were evaluated at the fuel-bed surface and compared to the measurements reported in [17]. The flame-zone depth was evaluated from the distribution of the absorption coefficient σ_G that depends on the gas mixture temperature and on the amounts of soot and of evaporation and combustion products (CO_2 and H_2O) [21] according to the following relation:

$$\sigma_G = 0.1(X_{CO2} + X_{H2O}) + 1862 f_v T \tag{7}$$

Where T is the gas mixture temperature, f_v is the soot volume fraction, and X_{CO2} and X_{H2O} are the mole fractions of CO_2 and H_2O respectively. This choice was motivated by the fact that the contours of the absorption coefficient define the boundaries of sooty flame that would be most visible in the experiments. Thus, figure 15 shows the flame area obtained numerically in the case of Exp. 10 and Exp. 24, and the flame-zone depth D was estimated from the horizontal extent of contour $\sigma_G = 1$. For each considered experiment, the value of the flame-zone depth

D was thus evaluated at different time steps and the average value is reported in Tab. 2; we notice that a satisfactory agreement is globally obtained with the rough measurements reported in [17].

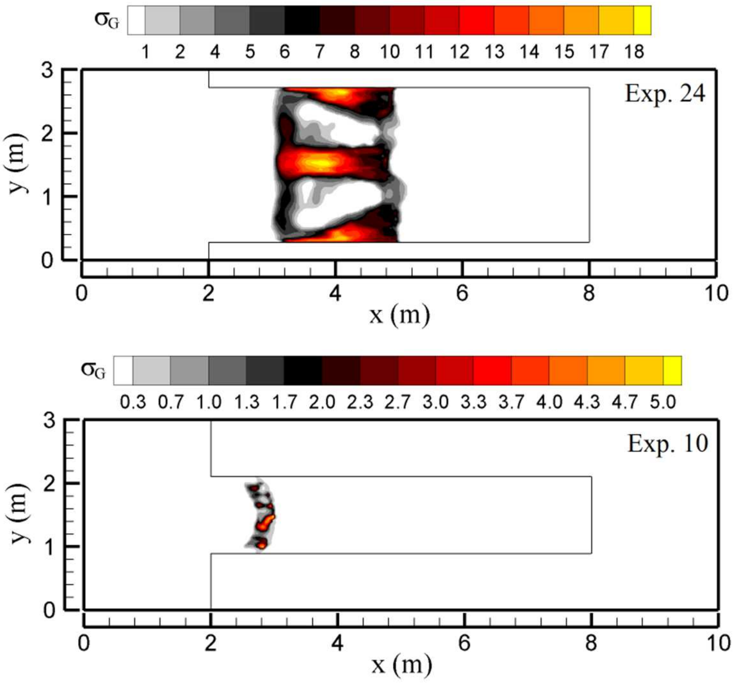

Fig. 15. Distributions of the absorption coefficient σ_G given by Eq. (7) at the surface of the fuel-bed (z = 0.203 m), obtained at t = 25 s in the case of Exp. 24 and Exp. 10 (see Tab. 1 for details).

Exp. No. as in [17]	10	18	19	24	25	26
ROS ($m.s^{-1}$) – Exp.	0.0119	0.0299	0.054	0.107	0.088	0.066
ROS ($m.s^{-1}$) – Sim.	0.0350	0.0380	0.050	0.111	0.087	0.081
f (Hz) – Exp.	1.269	1.195	1.643	1.350	2.449	1.162
f (Hz) – Sim.	1.084	1.258	1.600	1.252	1.760	1.070
n_w – Exp.	3	3	2	2	3	4
n_w – Sim.	1	2	2	2	3	3
D (m) – Exp.	0.2	0.2	0.4	1.2	0.5	0.3
D (m) – Sim.	0.172	0.259	0.751	1.448	0.392	0.192

Tab. 2. Comparison of the ROS, dominant frequency f of flame fluctuations, fire-front structure wavelength n_w, and the horizontal flame-zone depth D, obtained numerically using FIRESTAR3D and experimentally for the different experiments shown in Tab. 1.

4. Grassland fire spread with quasi-infinite fire front

4.1. Computational domain and numerical parameters

To reproduce the conditions similar to those encountered in the case of a quasi-infinite fire front and to avoid the border effects induced by a finite-length ignition line on the fire behavior [10, 14], the numerical simulations were carried out using periodic boundary conditions along the two lateral sides of the computational domain [12], as shown in Fig. 16. The length L of the computational domain was increased with the wind speed from 120 m up to 600 m in order to reach a steady rate of spread, while the fire front is still far enough from the end of the domain. The homogeneous vegetation layer (similar to a tall grass) is located at 20 m from the domain inlet and has the following main properties [26, 55]: vegetation height $\delta = 0.7$ m, fuel volume-fraction $\alpha_S = 0.002$, surface-to-volume ratio $\sigma_S = 4000$ m^{-1}, dry material density $\rho_S = 500$ kg.m^{-3}, moisture content $M = 5\%$, solid-fuel particles are assumed to have cylindrical shape and to behave as a black body. The simulations were carried out for seven values of the 10-m open wind speed $U_{10} = 1$, 3, 5, 8, 10, 12, and 16 m.s^{-1}. These velocities were measured at the domain inlet, 10 m above ground.

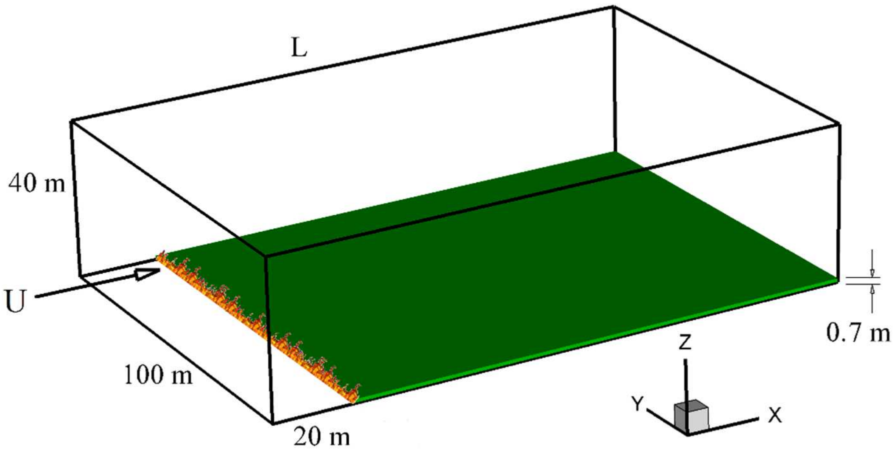

Fig. 16. Perspective view showing the dimensions of the computational domain and of the vegetation cover used in the case of grassland fire spread with quasi-infinite fire front, the ignition line is 2 m wide.

As in the case of wind-tunnel fires, before activating the burner, the hydrodynamic module of the code was run long enough until reaching a statistically quasi-steady state. During this phase, homogeneous Neumann boundary conditions were imposed at the top, inlet, and outlet boundaries of the computational domain for all primary variables of the problem except for y and z-velocity components that were set to zero. In addition, a negative pressure gradient is applied in the wind direction (Ox) and automatically adjusted to obtain the desired 10-m open wind speed. This procedure allowed collecting the turbulent fields at the open boundaries, and these fields were then used during the burning phase. Once the flow had reached a statistically-steady state, the burner was activated along an ignition line by injecting CO gas at 1600 K in from the bottom boundary of the domain according to Eq. (1). The burner was activated during 25 s (at most) or until consuming a fuel mass equal to that available above the burning area.

The results presented in this section were obtained using a LES turbulence model for the resolution of conservation equations of mass, momentum, energy, and species. For all wind speeds, the same mesh size was used in the y-z plane: for the solid phase a uniform grid with $(\Delta y, \Delta z) = (0.25 \text{ m}, 0.035 \text{ m})$ was used, while for the fluid phase a uniform grid with $(\Delta y, \Delta z) =$

(0.5 m, 0.07 m) was used within the vegetation before being gradually coarsened in the vertical direction. Both the solid-phase grid and the fluid-phase one were characterized by cells sizes below the extinction length scale [6] within the vegetation given by $4/\alpha_S \sigma_S$ and equal to 0.5 m in this case. A uniform mesh was used in the x direction but its size was increased with the wind speed: for the solid phase, the mesh size varied from $\Delta x = 0.25$ m for $U = 1$ m.s^{-1} up to $\Delta x = 0.5$ m for $U = 16$ m.s^{-1}, the mesh size of the fluid phase was twice that of the solid one.

The time step varied between 0.001 s and 0.01 s in the adaptive time-stepping strategy and the level of truncation error was set to 10^{-4}. At each time step, the solution is assumed to be obtained when the residuals of all conservation equations had reached 10^{-4} in normalized form. As a rough estimation of the computational cost, the simulation of 30 seconds of fire propagation required about 200 hours of CPU time on a 24-processor shared-memory workstation.

4.2. Results and discussion

The description of the results is limited in this section to the fire regime, the ROS, the fire intensity, and the characteristic wavelength of the fire-front structure for different wind speeds. 3D views of the fire propagation obtained for $U_{10} = 1$ m.s^{-1} and 10 m.s^{-1} are shown in Fig. 17. With a Byram's convective number nearly equal to 7096 for $U_{10} = 1$ m.s^{-1} and 3.6 for $U_{10} = 10$ m.s^{-1}, these two wind speed values cover the two regimes of propagation, i.e. plume dominated and wind driven. At low wind speed, the plumes rise is not noticeably affected by the action of the cross wind. In this case the fire front can be assimilated to an obstacle, and the air flow is deflected vertically by the plume. On the other hand, figure 17 shows how a stronger wind ($U_{10} = 10$ m.s^{-1}) affects more significantly the rise of the plumes by crossing the fire front and pushing the hot gases toward the unburned vegetation; this results for a wind-driven fire in a significant increase of the fire-front depth.

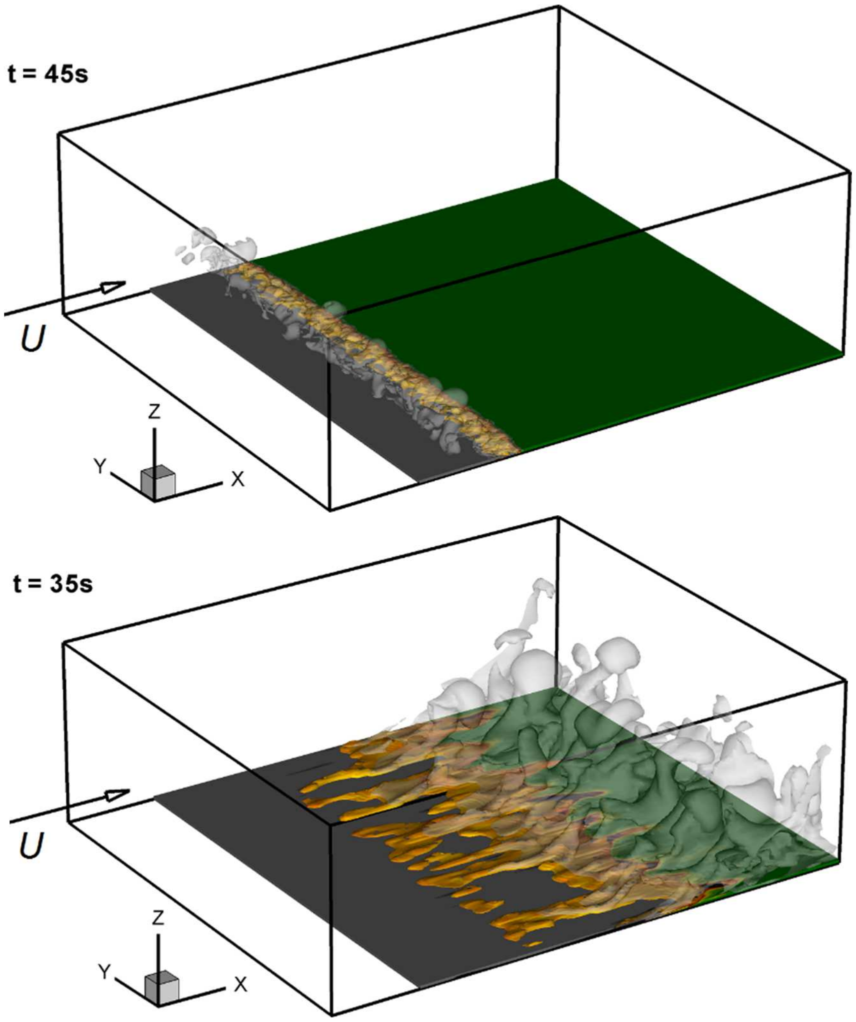

Fig. 17. 3D view of an isovalue surface of the soot volume fraction (10^{-6}) colored by the gas temperature (in yellow) and an isovalue surface of the water mass fraction (10^{-3}) (in grey with 50% of transparency) obtained in the case of grassland fire for U_{10} = 1 m.s^{-1} (top) and U_{10} = 10 m.s^{-1} (bottom), showing the effect of wind speed on the fire dynamics.

The significant effect of the wind speed is further illustrated by Fig. 18. We notice the important fresh air aspiration from the open boundaries to the vicinity of the fire front supplying the thermal plume. Moreover, this reverse flow is at the origin of the cooling of the unburned solid fuel located ahead of the fire front. The effect of the applied cross wind (U_{10} = 1 m.s^{-1}) is not visible on the flow field, and the thermal plume is tilted in the opposite direction to the fire propagation. For a stronger wind condition (U_{10} = 10 m.s^{-1}), the structure of the air flow is less affected by the fire front as shown in Fig. 18 (bottom), and this effect is limited to a local upward movement in the plume resulting from a local expansion of the hot gas mixture. The streamlines show clearly the possibility for the air flow to cross the fire front structured vertically in crests and troughs. The simulation of this fire feature is not possible with a 2D assumption, because in 2D the fire front represents a uniform thermal barrier preventing the air flow to cross the fire front.

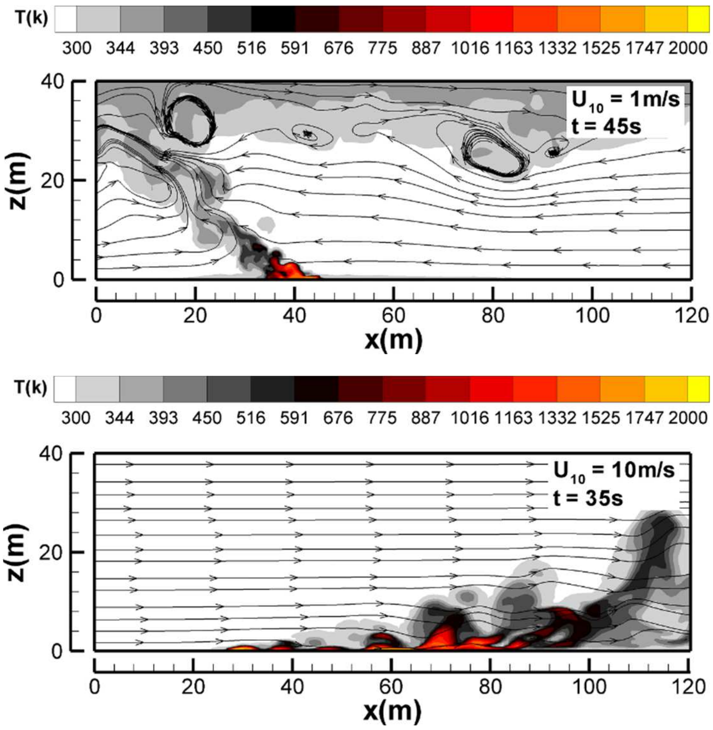

Fig. 18. Temperature field and streamlines of the gaseous phase, obtained in the case of grassland fire in the vertical median plane (y = 50 m) for U_{10} = 1 m.s^{-1} (top) and U_{10} = 10 m.s^{-1} (bottom), corresponding to the 3D fields shown in Fig. 17.

As in the wind-tunnel fires case, the ROS was estimated from the slope of the average position of the pyrolysis front at the surface of the vegetation cover, and shown in Fig. 19 versus with the 10-m open wind speed, where the experimental data were obtained from Cheney et al. [10, 57]. A Numerical study [56] had shown that the ROS increases with the ignition-line length L_i, before reaching an asymptotic value for L_i > 200 m. The relatively large dispersion of the experimental measurements can result from the unsteady nature of the wind flow [5]. On the other hand, the reported experimental data for $U_{10} \geq 8$ m.s^{-1} [57] were estimated from measurements recorded during real wildfires with significantly large fire front, but for which wind speed and vegetation characteristics are not under control as in experimental fires. For low to moderate U_{10} values (up to 6 m.s^{-1}), FIRESTAR3D results compare well with experimental data and with other predictions, and we can observe a quasi-linear evolution of the ROS. For $U_{10} \geq 8$ m.s^{-1}, the results are consistent with the predictions of other models (FIRETEC and WFDS) and with the experiments, despite the relative dispersion of the experimental measurements which prevents a significant comparison. For wildfires propagating under relatively strong wind conditions, we cannot exclude other factors than fuel properties itself, such as the unsteady nature of the wind flow (gusts) and the fact that burning particles (brands) could be ripped and transported by the wind flow ahead of the main fire front. These factors (not represented here) can play a significant role in the fire propagation.

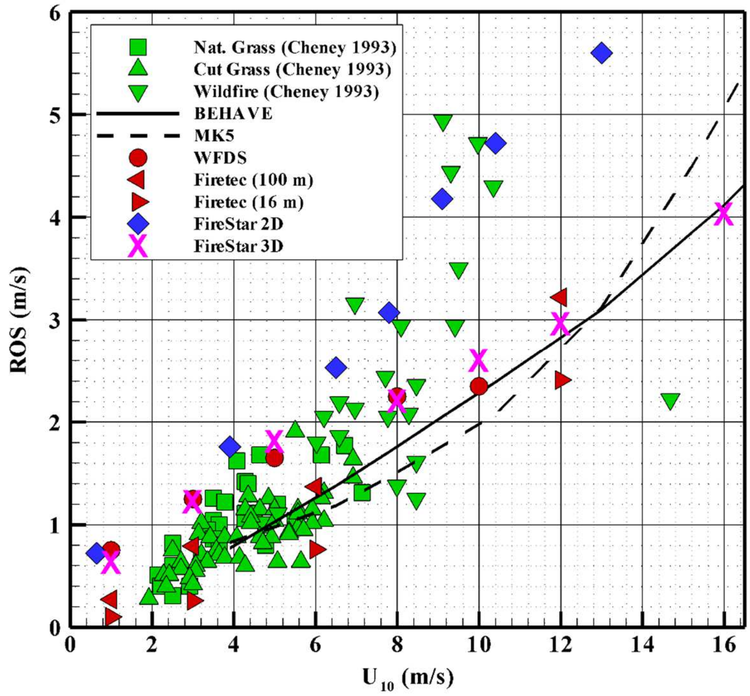

Fig. 19. Rate of fire spread (ROS) through a uniform grassland obtained for different 10-m open wind speeds. The results of FIRESTAR3D are compared to those obtained experimentally by Cheney et al., 1995, 1998 [10, 57], using the empirical model MK5 [57], the semi-empirical model BEHAVE+ [59], 3D numerical models FIRETEC [56] and WFDS [11], and the 2D numerical model FIRESTAR2D [26].

As in the wind-tunnel fires case, the heat release rate (HRR) was computed according to Eq. (6) and the fireline intensity is obtained from $I = HRR_{ss}/ L_i$, where HRR_{ss} is the average value of *HRR* obtained at steady state and L_i = 100 m in this case is the fireline length. As shown by Fig. 20, the present numerical results are compared (using the same set of physical parameters) to the predictions obtained using the operational models MK5 and BEHAVE+ and to the predictions of the 2D numerical model FIRESTAR2D. We have also reported some evaluations extracted from direct observations of prescribed and wildland fires on the field [59]; in this case, the fire line intensity was estimated from a laboratory measurement of the heat of combustion, by assuming that 100% of the solid fuel was consumed in the fire and that the rate of spread was constant. All the numerical simulations of grassland fires performed in this study, were characterized by a fire intensity larger than 6 $MW.m^{-1}$. In a fire fighting context, this value corresponds more or less to the efficiency limit of aerial means for the direct attack of a head fire (ranging between 3 and 10 $MW.m^{-1}$ depending on the spotting activity) [61]. The transition between a high and a very high fire danger index corresponds to a fire intensity of 6 $MW.m^{-1}$. The results of almost all the considered cases (except U_{10} = 1 $m.s^{-1}$) are located above this threshold value, which means that, even if the wind speed remains quite moderate, the fire can exhibit a very dangerous behavior because the fuel moisture content is very low (5%).

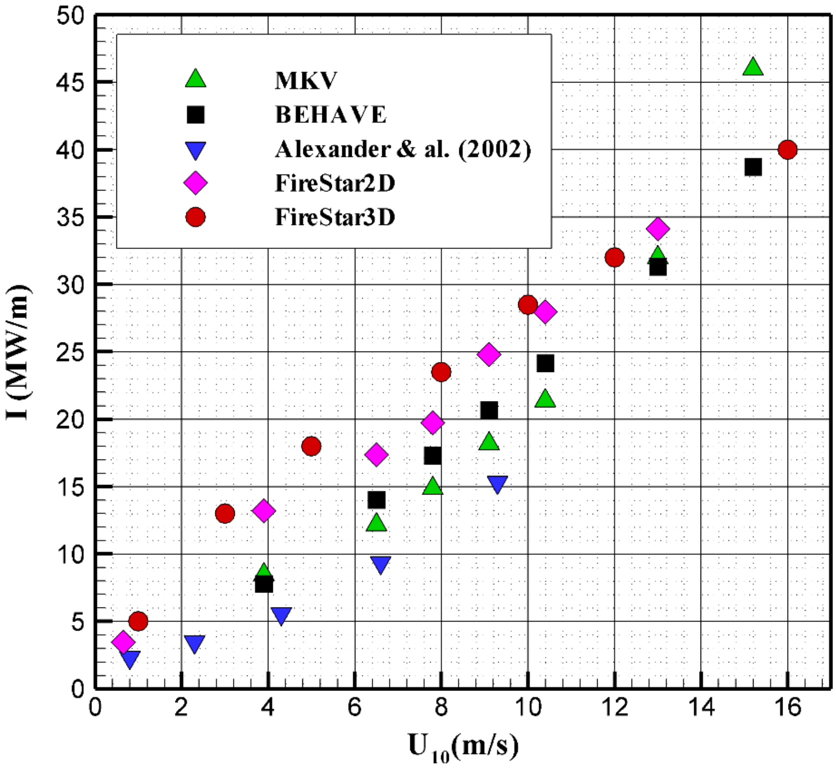

Fig. 20. Fireline intensity for fire propagation through a uniform grassland obtained for different 10-m open wind speeds. The results of FIRESTAR3D are compared to those obtained experimentally by Alexander et al 2002 [60], using the empirical model MK5 [58], the semi-empirical model BEHAVE+ [59], and the 2D numerical model FireStar2D [26].

As shown by Fig. 21, wind speed has a main effect on the heterogeneity of the fire front and its crest-and-trough structure, where it is obvious that the average distance between crests increases with the wind speed. This could be described as follows: for low wind speeds, the air flow behind the flame zone is vertically deflected by the buoyant force of the hot plumes and hardly break the fire front. In return for stronger wind conditions, the structure of the fire front is noticeably affected by the action of the cross wind that creates larger cavities with long wavelength along the fire front. Through these cavities, hot gases cross the fire front and heat up the fuel-bed ahead of it, resulting in a significant increase of the fire-front depth, and consequently of the fire intensity. We can notice that the structure of the fire front highlighted in the numerical simulations, are very similar to the experimental observations done both at the field scale and at the laboratory scale (see Fig. 22). We can also notice that this unsteady flow structure is typical to what can be observed during the development of a thermo-convective instability.

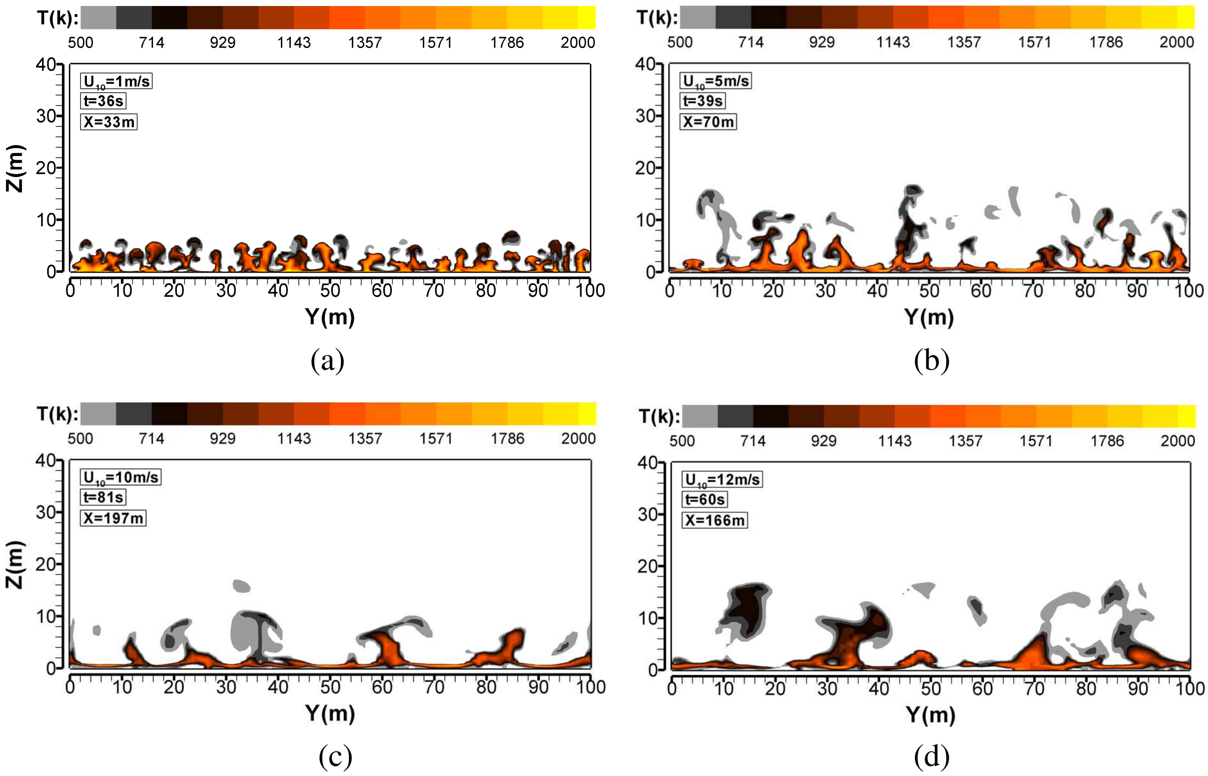

Fig. 21. Temperature patterns in the vertical (*y*,*z*) plane at the average pyrolysis front position obtained in the case of grassland fire for different wind speeds.

Fig. 22. Front view of the fire front from experiments carried in laboratory (on top) and on the field (on bottom) (Laboratoire Sciences Pour l'Envionnement, Université de Corse) [63].

5. Similitude in fire-front dynamics

As suggested in [16, 17], laboratory-scale fire spread could extend readily to full-scale field proportions as far as fire-front structure is concerned. To check this assumption, non-dimensional numbers characterizing the fire-front dynamics are evaluated both in the case of wind-tunnel fires and in the case of grassland fires. Hence, Byram's convection number (N_c) number and Froude's number (Fr), defined by Eqs. (1) and (8) respectively, are determined for all the considered case. Based on the main wavelength λ, Froude's number (Fr) characterizes the fire-front structure and represents the ratio between the wind inertial force and the plumes buoyant force . Byram's convection number characterizes the fireline intensity I and represent also the ratio between the power of buoyancy and the inertial power of the wind.

$$Fr = \frac{(U - ROS)^2}{g\,\lambda} \tag{8}$$

In the case of grassland fires, the characteristic wavelength λ could not be determined visually by counting the number of troughs as in the case of wind-tunnel fires. For grassland fires, a direct Fourier transform was performed of the temperature profile obtained along the fireline, 2 m above the fire front, and the dominant wavelength was determined. This operation is performed during steady-state fire propagation and with a time interval of 1 s. The wavelength λ characterizing the fire front heterogeneity is then determined as the average value of the wavelengths obtained at different times.

As mentioned in the introduction, wind-driven fires are characterized by small values of Byram's number (typically $N_C < 2$), while large values are obtained in the case of plume-dominated fires (typically $N_C > 10$) [7, 9]. For example, in the case of grassland fires, $N_C = 7096$ for $U = U_{10} = 1$ m.s^{-1} (plume-dominated fire), while $N_C = 1.3$ for $U = U_{10} = 16$ m.s^{-1} (wind-driven fire). In return, in the case of wind-tunnel fires, in our simulations N_C varied from 100 (for $U = 0.89$ m.s^{-1}) to 4657 (for $U = 0.22$ m.s^{-1}), while in the experiments N_C varied between 16 and 25460. Thus all considered cases of wind-tunnel fires are plume-dominated.

Froude's number is plotted in Fig. 23 versus Byram's convection number for all simulated wind-tunnel and grassland fires. Figure 23 also shows the experimental results obtained by Finney et al. [16, 17], for which the fireline intensity I used in Eq. (1) was estimated as $I = W \times ROS \times \Delta H$, where $W = \rho_S \alpha_S \delta$ (kg.m^{-2}) is the fuel loading and ΔH is the heat yield of the cardboard fuel (estimated at about 14480 kJ.kg^{-1} [62]). It was foreseeable to find that Froude's and Byram's numbers were well correlated with a certain exponent (equal here to 0.613 for the experimental data), since they both compare the ratio between buoyancy and wind inertia. It was however interesting is to find that the correlation is almost the same at a small scale (experimental and numerical wind-tunnel fires) and at large scale (numerical grassland fires), which validate the similitude in the fire-front dynamics (fireline intensity and the fire-front structure) between the two scales. The good agreement between the simulations and the experimental data also validate the levels of the fireline intensities obtained in the case of wind-tunnel fires.

Note also that the scaling (evaluating on the whole data) between Froude's and Byram's numbers in Fig. 23 can be approximated simply by $Fr = N_C^{-2/3}$. Using Eqs. (1) and (8), this approximation results in the expression given by Eq. (9) for the characteristic wavelength of the fire-front structure.

$$\lambda \approx \left(\frac{2\,I}{\rho\, C_P T_0}\right)^{2/3} \frac{1}{g^{1/3}} \tag{9}$$

It is interesting to point out the characteristic wavelength λ does not depend explicitly on the wind speed or the ROS, but only on natural convection-related parameters. Certainly, λ depends on the wind speed as shown previously by Fig. 21, but this dependence is implicit through the fireline intensity. Another remarkable point is that this scaling law is similar to those relating the flame height and the heat release rate for a fire plume (i.e. a fire dominated by buoyancy effects) [64, 65].

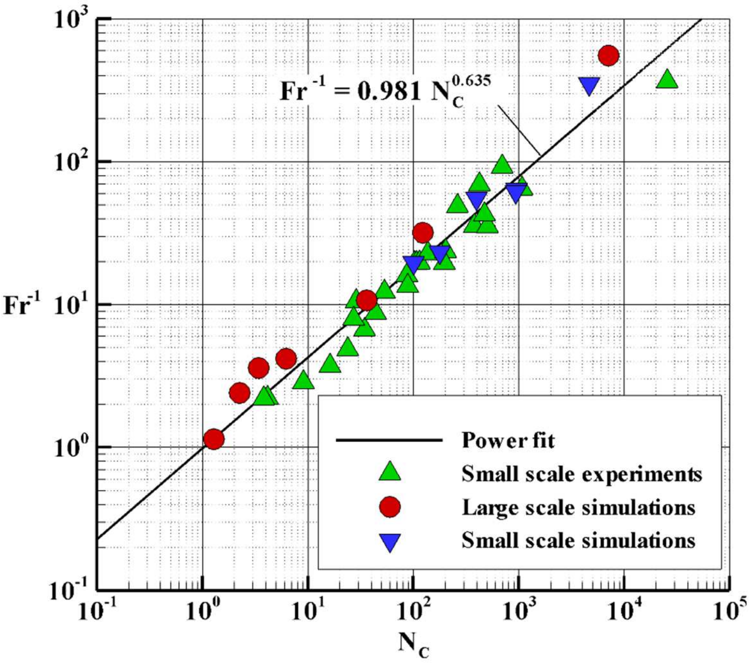

Fig. 23. Froude's number based on the wavelength characterizing the fire-front structure versus Byram's convective number. The results of FIRESTAR3D obtained in the case of grassland fire and in the case of wind-tunnel are compared to those obtained experimentally [16, 17].

6. Conclusions

The objective of this research was to identify the physical mechanisms responsible for the 3D structure of a fire front propagating through a homogeneous fuel-bed, and to investigate the similitude in fire-front dynamics at small and large scales. For this purpose, numerical simulations of fire spread were carried out using the fully physical, multiphase model FIRESTAR3D, at laboratory and field scales. At laboratory scale, many experiments of fire spread through laser-cut cardboard fuel-beds, carried out in wind tunnel at Missoula Fire Sciences Laboratory, were modeled and reproduced numerically. At a large scale, simulations of grassland fires with a quasi-infinite fire front were carried out for different wind speeds using periodic conditions at the lateral boundaries. The comparison with the experimental data showed that FIRESTAR3D predicts correctly the ROS and the fireline intensity. In addition, in the case of wind-tunnel fires, FIRESTAR3D was able to predict satisfactorily the main frequency *f* of flame fluctuations recorded experimentally, the horizontal flame-zone depth, as well as the predominant wavelength λ characterizing the fire-front structure in the transverse direction. This characteristic wavelength was obtained in the case of grassland fires by FFT of the gas-mixture temperature above the fireline.

Both at small and large scales, simulations highlighted the effects of the wind speed on the ROS and on the fireline intensity, as well as the competition between the buoyant forces of the thermal plumes and the inertial forces of the wind. This competition is at the origin of the crest-and-trough structure of the fire front. Fire-front dynamics was characterized by Byram's number (N_C) based on the fireline intensity and Froude's number (Fr) based on the characteristic wavelength λ of the fire-front structure. All the reported results (numerical and experimental, wind-tunnel and grassland fires) were gathered-up by a simple relationship, $Fr = N_C^{-2/3}$, that defines consequently the similitude in fire-front dynamics between laboratory fires and full-scale field fires. This simple scaling law revealed also that the main wavelength λ characterizing the 3D structure of the fire front only depends on natural convection-related parameters and increases as power 2/3 of the fireline intensity.

Many other fundamental aspects of the wildfire dynamic are not well understood, such as the role played by the field slope (and the competition between the wind and the slope when their directions are not aligned), the impact of the fuel moisture content (its threshold effect in the burn/no burn process, the linear or exponential decay of the rate of spread). This research showed how, in complement to experimental investigations, detailed physical models (such as FIRESTAR3D) could help understanding the basic physical mechanisms governing the behavior of wildfires.

Acknowledgments

The authors thank Aix-Marseille University for granting access to the HPC resources funded by Equip@Meso project (ANR-10-EQPX-29-01) of “Investissements d’Avenir” program. The authors also thank Missoula Fire Science Laboratory staff, and in particular Mark Finney, for their permission to publish two photos taken during a visit to the Laboratory and for providing the required unpublished data to conduct the simulations. The authors thank as well the staff of "Laboratoire Sciences Pour l’Environnement" (SPE) at the University of Corsica, and in particular Thierry Marcelli, Frédéric Morandini, Carmen Awad, Lucile Rossi, and Jean-Louis Rossi, for their permission to publish two photos of experimental fires.

References

[1] R. Steffens, The Camp fire burns Paradise, and we must act, Wildfire 27 (2018) 6–7.

[2] Ch. D. O’Connor, D.E. Calkin. Engaging the fire before it starts: a case study from the 2017 Pinal fire (Arizona), Wildfire 28 (2019) 14–18.

[3] M.A. Finney, J.D. Cohen, S.S. McAllister, W.M. Jolly, On the need for a theory of wildland fire spread, Int. J. Wildl. Fire. 22 (2013) 25–36.

[4] D. Morvan, Numerical study of the effect of fuel moisture content (FMC) upon the propagation of a surface fire on a flat terrain, Fire Saf. J. 58 (2013) 121–131.

[5] D. Morvan, Wind effects, unsteady behaviors, and regimes of propagation of surface fires in open field, Combust. Sci. Technol. 186 (2014) 869–888.

[6] D. Morvan, Physical phenomena and length scales governing the behaviour of wildfires: A case for physical modelling, Fire Technol. 47 (2011) 437–460

[7] D. Morvan, N. Frangieh, Wildland fires behaviour: Wind effect versus Byram's convective number and consequences upon the regime of propagation, Int. J. Wildl. Fire. 27 (2018) 636–641.

[8] G.M. Byram, Combustion of forest fuels, in: Davis, K.P.(Eds.), Forest Fire Control and Use, McGraw-Hill, New York 1959, pp. 90–123.

[9] R.M. Nelson, Re-analysis of wind and slope effects on flame characteristics of Mediterranean shrub fires, Int. J. Wildl. Fire. 24 (2015) 1001–1007.

[10] N.P. Cheney, J.S. Gould, Fire growth in grassland fuels, Int. J. Wildl. Fire. 5 (1995) 237–247.

[11] W. Mell, M.A. Jenkins, J. Gould, P. Cheney, A physics-based approach to modelling grassland fires, Int. J. Wildl. Fire. 16 (2007) 1–22.

[12] J.M. Canfield, R.R. Linn, J.A. Sauer, M. Finney, J. Forthofer, A numerical investigation of the interplay between fireline length, geometry, and rate of spread, Agric. For. Meteorol. 189–190 (2014) 48–59.

[13] N. Frangieh, D. Morvan, S. Meradji, G. Accary, O. Bessonov, Numerical simulation of grassland fires behavior using an implicit physical multiphase model, Fire Saf. J. 102 (2018) 37–47.

[14] R.R. Linn, J.M. Canfield, P. Cunningham, C. Edminster, J.L. Dupuy, F. Pimont, Using periodic line fires to gain a new perspective on multi-dimensional aspects of forward fire spread, Agric. For. Meteorol. 157 (2012) 60–76.

[15] T.W. Beers, the Interaction of Wind and Fire, Boundary-Layer Meteorol. 54 (1991) 287–308.

[16] M.A. Finney, J.D. Cohen, J.M. Forthofer, S.S. McAllister, M.J. Gollner, D.J. Gorham, K. Saito, N.K. Akafuah, B.A. Adam, J.D. English. Role of buoyant flame dynamics in wildfire spread, Proc. Natl. Acad. Sci. (PNAS) 112 (2015) 9833-9838.

[17] M.A. Finney, J. Forthofer, I.C. Grenfell, B.A. Adam, N.K. Akafuah, K. Saito, A study of flame spread in engineered cardboard fuelbeds: Part I: Correlations and observations, Proc. (Int.) Symp. Scale Model. (ISSM) 7 (2013).

[18] J.L. Dupuy, R.R. Linn, V. Konovalov, F. Pimont, J.A. Vega, E. Jiménez, Exploring three-dimensional coupled fire–atmosphere interactions downwind of wind-driven surface fires and their influence on backfires using the HIGRAD-FIRETEC model, Int. J. Wildl. Fire. 20 (2011) 734-750.

[19] P. Clavin, G. Searby. Combustion waves and fronts in flows, Cambridge University Press, (2016).

[20] J.L. Dupuy, D. Morvan. Physical modelling of forest fire behaviour in a fuel break, Int. J. Wildl. Fire. 14 (2005) 141-151.

[21] D. Morvan, G. Accary, S. Meradji, N. Frangieh, O. Bessonov. A 3D physical model to study the behaviour of vegetation fires at laboratory scale, Fire Saf. J. 101 (2018) 39-52.

[22] A.M. Grishin, Mathematical Modeling of Forest Fires and New Methods of Fighting them, in: F. Albini (Eds.), Publishing House of the Tomsk University, Tomsk, Russia, 1997.

[23] D. Morvan, J.L. Dupuy, Modeling of fire spread through a forest fuel bed using a multiphase formulation, Combust. Flame 127 (2001) 1981-1994.

[24] D. Morvan, J.L. Dupuy, Modeling the propagation of a wildfire through a Mediterranean shrub using a multiphase formulation, Combust. Flame 138 (2004) 199-210.

[25] D. Morvan, S. Meradji, G. Accary, Wildfire behavior study in a mediterranean pine stand using a physically based model, Combust. Sci. Technol. 180 (2008) 230–248.

[26] D. Morvan, S. Meradji, G. Accary, Physical modelling of fire spread in Grasslands, Fire Saf. J. 44 (2009) 50–61.

[27] A. Favre, L.S.G. Kovasznay, R. Dumas, J. Gaviglio, M. Coantic, La turbulence en mécanique des fluides. Gauthier-Villars, 1976.

[28] G. Cox, Combustion Fundamentals of Fire, Academic Press, 1995.

[29] V. Yakhot, L.M. Smith, The renormalization group, the epsilon-expansion and derivation of turbulence models, J. Sci. Comput. 7 (1992) 35–61.

[30] S.A. Orszag, I. Staroselsky, W.S. Flannery, Y. Zhang, Introduction to renormalization group modeling of turbulence, Simul. Model. Turbul. Flows. (1996) 155–183.

[31] K. Gavrilov, Numerical Modeling of atmospheric layer flow over forest canopy, PhD Thesis, Aix-Marseille University II, 2011.

[32] R.J. Kee, F.M. Rupley, J.A. Miller, The CHEMKIN thermodynamic data base. Technical report, Sandia National Laboratories, 1992.

[33] B.F. Magnussen, B.H. Mjertager, On mathematical modeling of turbulent combustion, Combust. Sci. Technol. 140 (1998) 93–122.

[34] K.J. Syed, C.D. Stewart, J.B. Moss, Modelling soot formation and thermal radiation in buoyant turbulent diffusion flames, Symp. (Int.) Combust. 23 (1991) 1533–1541.

[35] J.B. Moss, Turbulent Diffusion Flames, in: G. Cox (Eds.), Forest Fire Control and Use, Academic Press, London, UK, 1990.

[36] J. Nagle, R.F. Strickland-Constable, Oxidation of carbon between 1000–2000°C, Proc. Fifth Conf. Carbon 5 (1962) 154–164.

[37] F.P. Incropera, D.P. DeWitt, Fundamentals of Heat and Mass Transfer, John Wiley and Sons, 1996.

[38] R. Siegel, J.R. Howell, Thermal Radiation Heat Transfer, 3rd Ed., Hemisphere Publishing Corporation, Washington D.C, 1992.

[39] S.V. Patankar, Numerical Heat Transfer and Fluid Flow, Hemisphere Publishing, New York, 1980.

[40] H.K, M. Versteeg W, An Introduction to Computational Fluid Dynamics, the Finite Volume Method, Prentice Hall, 2007.

[41] Y. Li, M. Rudman, Assessment of higher-order upwind schemes incorporating FCT for convection-dominated problems, Numer. Heat Transf. Part B Fundam. 27 (1995) 1–21.

[42] J.H. Ferziger, M. Peric, A. Leonard, Computational Methods for Fluid Dynamics, Springer-Verlag, 2002.

[43] M.F. Modest, Radiative Heat Transfer Academic Press, 2003.

[44] C.R. Kaplan, S.W. Baek, E.S. Oran, J.L. Ellzey, Dynamics of a strongly radiating unsteady ethylene jet diffusion flame, Combust. Flame. 96 (1994) 1–21.

[45] G. Accary, O. Bessonov, D. Fougere, S. Meradji, D. Morvan, Optimized parallel approach for 3D modelling of forest fire behaviour, in: V.E. Malyshkin (Ed.), PaCT 2007, LNCS, 4671 Springer, Heidelb, 2007, pp. 96–102.

[46] G. Accary, O. Bessonov, D. Fougere, K. Gavrilov, S. Meradji, D. Morvan, Efficient parallelization of the preconditioned conjugate gradient method, in: V.E. Malyshkin (Ed.), PaCT 2009, LNCS, 5968 Springer, Heidelb, 2009, pp. 60–72.

[47] A. Khalifeh, G. Accary, S. Meradji, G. Scarella, D. Morvan, K. Kahine, Three-dimensional numerical simulation of the interaction between natural convection and radiation in a differentially heated cavity in the low Mach number approximation using the discrete ordinates method, 4th UAE International Proceeding Conference in Thermal Engineering: Theory and Application, Abu Dhabi (2009).

[48] G. Accary, S.Meradji, D. Fougère, D. Morvan, Towards a numerical benchmark for 3D mixed-convection Low Mach number flows in a rectangular channel heated from below, J. Fluid Dyn. Mater. Sci. 141 (2008) 1–7.

[49] K. Gavrilov, G. Accary, D. Morvan, D. Lyubimov, S. Méradji, O. Bessonov, Numerical simulation of coherent structures over plant canopy, Flow, Turbul. Combust. 86 (2011) 89–111.

[50] K. Gavrilov, D. Morvan, G. Accary, D. Lyubimov, S. Meradji, Numerical simulation of coherent turbulent structures and of passive scalar dispersion in a canopy sub-layer, Comput. Fluids. 78 (2013) 54–62.

[51] W.R. Catchpole, E.A. Catchpole, B.W. Butler, R.C. Rothermel, G.A. Morris, D.J. Latham, Rate of spread of free-burning fires in woody fuels in a wind tunnel, Combust. Sci. Technol. 131 (1998) 1–37.

[52] M. A. Finney, Personal communication.

[53] S.U. Islam, C.Y. Zhou, A. Shah, P. Xie, Numerical simulation of flow past rectangular cylinders with different aspect ratios using the incompressible lattice Boltzmann method, J. Mech. Sci. Technol. 26 (2012) 1027–1041.

[54] G. Schewe, Reynold number effect in flow around a rectangular cylinder with aspect ratio 1:5, Journal of fluid and structures 39 (2013) 15-26.

[55] M. Rahnama, S. M. Hashemian, and M. Farhadi, Forced convection heat transfer from a rectangular cylinder: effect of aspect ratio, ISTP-16, Prague, 2005.

[56] R.R. Linn, P. Cunningham, Numerical simulations of grass fires using a coupled atmosphere-fire model: Basic fire behavior and dependence on wind speed, J. Geophys. Res. Atmos. 110 (2005).

[57] N.P. Cheney, J.S. Gould, W.R. Catchpole, Prediction of fire spread in grasslands, Int. J. Wildl. Fire. 8 (1998) 1–13.

[58] A. G. McArthur, Fire behaviour in eucalypt forests, Forest Research Institute, Leaflet No. 107, Canberra, Australia, 1967.

[59] R. C. Rothermel, A mathematical model for predicting fire spread in wildland fuels, USDA Forest Service Research Paper 40, INT, USA, 1972.

[60] M.E. Alexander ME and L. G. Fogarty, A pocket card for predicting fire behaviour in grasslands under severe burning conditions. Fire Technology Transfer Note 25, 2002.

[61] K.G. Kelvin, D.L. Martell, A review of initial attack fire crew productivity and effectiveness, Int. J. Wildl. Fire. 6(4) (1996) 199–215.

[62] G. Agarwal, G. Liu, and B. Lattimer, Pyrolysis and oxydation of cardboard, Proc. (Int.) of Fire Saf. Sci. 11 (2014) 124-137.

[63] T. Toulouse, L. Rossi, A. Campana, T. Celik, M.A. Akhloufi, Computer vision for wildfire research: An evolving image dataset for processing and analysis, Fire Saf. J. 92 (2017) 188–194.

[64] E.E. Zukoski Properties of fire plumes in Combustion fundamentals of fire, Ed. G. Cox (1996), 101-219, Academic Press.

[65] J.G. Quintiere Scaling application in fire research, Fire Saf. J. 15 (1989) 2-29.